Macroscopic traffic flow modeling with adaptive cruise control: Development and numerical solution

A. I. Delis[a,*], I. K. Nikolos[a], M. Papageorgiou[a]

[a]*School of Production Engineering & Management, Technical University of Crete, Chania, Greece*

Abstract

The incorporation of two macroscopic approaches reflecting Adaptive Cruise Control (ACC) and Cooperative Adaptive Cruise Control (CACC) traffic dynamics in a gas-kinetic (GKT) traffic flow model is presented. The first approach was recently analyzed in the literature aiming to describe the effects induced by the ACC and CACC systems due to changes of the speed of the leading car(s) by the introduction of an acceleration/deceleration term. The second approach is a novel one and is based on the introduction of a relaxation term that satisfies the time/space-gap principle of ACC or CACC systems. In both approaches, the relaxation time is assigned on multiple leading vehicles in the CACC case; whereas in the ACC case this relaxation time is only assigned to the direct leading vehicle. We numerically approximate the resulting models by an accurate and robust high-resolution finite volume relaxation scheme, where the nonlinear system of partial differential equations are first recast to a diagonilizable semi-linear system and are then discretized by a higher-order WENO scheme. Numerical simulations investigate the effect of the different ACC and CACC approaches to traffic flow macroscopic stability with respect to perturbations introduced in a ring road and to flow characteristics in open freeways with merging flows at an on-ramp. Following from the numerical results, it can be concluded that CACC vehicles increase the stabilization of traffic flow, with respect to both small and large perturbations, compared to ACC ones. Further, the proposed CACC approach can better improve the dynamic equilibrium capacity and traffic dynamics, especially at the on-ramp bottleneck.

Keywords: Traffic flow dynamics; Macroscopic traffic flow models; Cooperative adaptive cruise control; Hyperbolic conservation laws; Numerical simulation; Finite volume relaxation schemes

1. Introduction

Emerging technologies in the field of Vehicle Automation and Communication Systems (VACS), such as Adaptive Cruise Control (ACC) and Cooperative Adaptive Cruise Control (CACC) systems, are likely to revolutionize the way traffic flow will be controlled and optimized in the near

---

*Corresponding author. Tel.:+302821037751

Email address: adelis@science.tuc.gr (A. I. Delis)

future. Although such technologies have been developed to increase driver's comfort and safety, the continuously increasing use of such systems in the years to come will have a direct impact on the overall traffic flow. The widespread use of such systems can form a potential solution to the continuously increasing problem of traffic congestion, by using advanced control strategies to increase road capacity, stabilize the flow and accomplish an optimal usage of the available infrastructure. As a result, a new generation of Traffic Management (TM) strategies need to be developed and tested, which will allow for the optimal use and exploitation of such systems. To this end, the development of appropriate modeling tools for such systems should be a priority, to allow for the reliable and efficient simulation of their performance and of the effects they have on traffic flow; this would allow to optimize the relevant parameters and explore new strategies for VACS implementation.

An ACC system forces the vehicle to slow down when the leading vehicle has a lower speed and, reversely, allows the vehicle to accelerate to a pre-determined speed when the leading vehicle accelerates. In principle, the pre-specified parameters of an ACC system are the time-gap to the leading vehicle and the desired speed of the vehicle. The main aim of such a system is to liberate the driver from the need to adjust its speed to that of the leader. However, the application of ACC systems, and for certain parameter settings, may also induce negative effects on traffic flow dynamics. Hence, and in order to minimize potential negative effects, it is crucial to evaluate the impact of such systems on traffic flow dynamics in advance. Vehicles equipped with CACC systems have the ability of sharing traffic information via vehicular networks or wireless technologies that allow communication between such vehicles. CACC systems constitute a further development of the ACC technology which provides more accurate and faster real time information sharing among the equipped vehicles. Research has shown that CACC systems can potentially improve safety as well as the traffic dynamics (in terms of capacity, flow, average speed and speed variation), if widely adopted. Compared to ACC, the literature on CACC systems is still very premature and relevant studies, usually, do not explore the effects of CACC in traffic flow quantitatively in terms of throughput, capacity, and congestion reduction but aim on creating design frameworks, to optimize and standardize the use of such technology.

Although much work has been reported for the microscopic simulation of ACC/CACC systems at vehicle level, we refer for example to [1, 49, 8, 48, 9, 22, 23, 41, 34, 42, 2, 35, 36], model applications of macroscopic or gas kinetic traffic flow models for the simulation of VACS are relatively rare. However, the development of accurate macroscopic traffic flow models for the simulation of VACS will be of major importance in the future, for real-time prediction and control applications, when the percentage of CACC/ACC vehicles will have significantly increased thus affecting considerably the traffic dynamics. As macroscopic models require less computational resources and simpler calibration effort than microscopic ones, they can be easily and more efficiently combined with optimization algorithms, either for parameter estimation or for optimization purposes. In [43] a design approach for an ACC strategy in an Automated Highway System based on macroscopic traffic flow stability analysis was presented. Using a linearized stability analysis, it was shown that the traffic flow equilibrium state was marginally stable under a constant time headway (CTH) policy. Moreover, in [51] a macroscopic model was presented with velocity saturation for traffic flow where vehicles are controlled with ACC spacing policy. Additionally, a non-linear stability crite-

2

rion was derived, while the stability results provided sufficient and necessary conditions for ACC traffic flow stability. In [25] and [20] the macroscopic formulation of a kinetic model to variable speed control was applied using Variable Message Signs (VMS). In the first work a sliding mode controller was applied, being able to eliminate stop-and-go waves, as the controller increases the flow above some density and decreases it for the flow below this density. In the second work a similar approach was adopted, and VMS were used to inform drivers of slower traffic ahead. They assumed that drivers decrease their desired velocity when control is active and applied the variable average desired speed in the macroscopic implementation of the model. As a result, the occurrence of the so-called phantom traffic jams was prevented, as long as the speed adaptation by the drivers was sufficiently large. The impact of ACC concepts on the macroscopic level of traffic flow modeling was also considered in [10]. The simulation results showed that at lower time headways there is an improvement of traffic conditions (higher flow rate, faster dissolution of the congestion), even with small penetration rates; up to a certain penetration rate the traffic flow rate is increasing whereas higher penetration rates do not provide additional benefits.

In [29] a continuum approach to model the dynamics of cooperative traffic flow was presented, where the cooperation is defined in a way that the equipped vehicle can issue and receive a warning massage when downstream congestion has been created. To this end, a multi-class gas-kinetic theory was extended to capture the adaptation of the desired speed of the equipped vehicles to the speed at the downstream congested traffic. Numerical tests indicated that the equipped vehicles contribute significantly to the stabilization of traffic flow, while increasing the fraction of equipped vehicles leads to a delay in traffic inflowing to the congested area and consequently results in a reduced shock-wave strength. In [30] the mixed operation of manual and ACC traffic flow was investigated, by deriving macroscopic multi-class traffic equations, obtained from a gas-kinetic model using the method of moments. A gas-kinetic macroscopic traffic flow model was further proposed in [31], based on a car-following one, to describe the dynamics of traffic where vehicles operate in the form of many platoons. A linear stability analysis showed a stabilization of the flow with respect to small perturbations. The analytic results were supported by the numerical simulation of an open freeway with an on-ramp bottleneck. In [33] the derivation of an improved macroscopic model for multi-anticipative driving behavior, using a modified gas-kinetic approach, was presented. Theoretical analysis and numerical simulations of the model were carried out to show the improved performance of the derived model over other existing multi-anticipative macroscopic models. In [32] a macroscopic model is proposed to describe the operations of CACC in the traffic flow. Using linear and nonlinear stability analysis it was found that CACC vehicles enhance the stabilization of traffic flow with respect to both small and large perturbations, compared to ACC vehicles, while numerical simulation supported the analytical findings. Further, from the linear analytical results, the relaxation term and the convection term counteracted the reinforcement instability mechanism. This lead to different propagation of the shock waves.

The present work aims to contribute to the macroscopic modeling of traffic flow consisting of ACC or CACC vehicles, along with appropriate numerical approximations; it builds on a previous work of the authors in [7] where a unified methodology was proposed for the numerical simulation of several, widely applied, second-order non-equilibrium macroscopic models. In [7], utilizing the

3

relaxation approximation, from [24], the nonlinear macroscopic traffic flow differential equations were transformed to a diagonilizable semi-linear problem. The resulting relaxation system was discretized using low- and high-resolution reconstructions in space which include a first-order upwind scheme, a second-order MUSCL scheme and a fifth-order WENO scheme. The main features of the proposed numerical approach are its simplicity, accuracy and robustness.

Here, the GKT second-order traffic flow model, [44, 15, 16, 47], is utilized, within the aforementioned computational framework, as a basis to import and access two alternative models for the macroscopic simulation of ACC/CACC traffic. The first model is the one proposed by Ngoduy [32], slightly modified and adapted, while the second one is a new approach, designed in order to take into account additional features of the ACC/CACC traffic. Both models are incorporated as source terms to the second ("momentum") equation of the system of partial differential equations forming the GKT model, which controls the speed dynamics. However, one major difference between the two approaches is that the ACC/CACC term in [32] contributes to the so-called convection term in the momentum equation whereas in our approach the corresponding term contributes to the relaxation term in the GKT model equations. Moreover, in our ACC and CACC modeling approach the time-gap parameter, which is an important characteristic of such systems, is explicitly taken into account.

Two main categories of simulation cases are presented in the numerical simulations to validate the performance of the two approaches and their effects on the traffic flow characteristics. The first one is for flows on a circular homogeneous freeway with respect to small and large perturbations. The second is the simulation of a freeway with an on-ramp bottleneck. Each approach has its own effects on the traffic flow dynamics, but, in general, both lead to the stabilization of the flow when disturbances are introduced. Both approaches lead to more anticipative driving behavior in congested traffic situations which leads to the suppression of instabilities. However, the ability to explicitly define the time-gap in our approach enables the model to simulate ACC/CACC flows with different time-gap settings, which lead to different dynamic behavior and equilibrium capacities. This ability also gives the opportunity to access the impact of the time-gap settings on traffic flow performance, as ACC/CACC systems increase driving comfort and safety but may have a negative impact on traffic flow depending on their parameters' settings.

We note here that, the main assumptions implied for the derivation and testing of the proposed ACC and CACC approach are the following; (a) the penetration rate of ACC/CACC-equipped vehicles is taken equal to 100% in this work, (b) all vehicles are assumed to be of the same class with the same characteristics, (c) all equipped vehicles are assumed to have the same parameter values for the ACC or CACC system they use and (d) the models are developed assuming single lane flow conditions i.e. no lane changing is assumed. All these simplifications are assumed as to isolate the behavior of the ACC and CACC modeling from other aspects of the traffic flow. Multi-lane and multi-class effects in the current framework will be the subject of future work, as our aim is to progressively built different aspects of VACS' characteristics into a unified macroscopic computational framework.

The main contributions of the present work can be summarized as follows: (a) to derive a novel macroscopic approach to incorporate the behavior of ACC and CACC equipped vehicles

into the GKT traffic flow model, (b) to compare its performance with the approach proposed by Ngoduy in [32] in various test cases, (c) to qualitatively assess its performance through the numerical simulations on various traffic flow scenarios, (d) to extensively validate the models through a proposed suite of relevant demanding test cases and (e) to demonstrate that the adopted numerical approach can effectively simulate different traffic flow phenomena for manually driven and ACC/CACC equipped vehicles for both utilized approaches.

2. The GKT model and adaptive cruise control

The macroscopic model implemented and extended here is the gas-kinetic-based traffic flow model (GKT model), which has been deduced from microscopic models describing driver-vehicle behavior in [44, 15, 16, 47]. A similar derivation can be found also in [4]. The GKT model has been shown to describe realistic characteristic properties of traffic flows. Furthermore, this model is able to describe the hysteretic phase transitions to congested states, that typically occur behind on-ramps, gradients, or other bottlenecks in busy freeways [13, 45].

In what follows, we will denote as functions in space, x, and time, t, $\rho(x, t)$ the vehicle or traffic density (number of vehicles per unit length), $u(x, t)$ the average speed and $q = \rho u$ the traffic flow rate (number of vehicles per unit time). We recast the GKT model in conservation law form with sources (also called a balance law), written as

$$\partial_t \rho + \partial_x (\rho u) = r_{rmp},\tag{1}$$

$$\partial_t (\rho u) + \partial_x \left(\rho u^2 + \theta \rho \right) = \rho \left(\frac{V_e^\star(\rho, u, \rho_a, u_a) - u}{\tau} \right) [1 - \beta F(\rho)] + h_{rmp} + \alpha \mathcal{V}_{acc}.\tag{2}$$

In (2) we have also incorporated the modeling of ACC and CACC cars in the terms $\alpha \mathcal{V}_{acc}$ and $[1 - \beta F(\rho)]$, which will be explained later; by setting $\alpha = \beta = 0$ in these terms, the GKT model equations for manually driven cars are obtained and will be explained first.

Following [47], the source term r_{rmp} in the continuity equation (1) denotes the effective source density from on-ramps (or off-ramps) with merging (diverging) length l_{rmp} and inflow $q_{rmp} > 0$ from (or outflow $q_{rmp} < 0$ to) the ramp, and is given as

$$r_{rmp}(x, t) = \begin{cases} \dfrac{q_{rmp}(t)}{l_{rmp}} & \text{if } x \text{ is within merging or diverging zones,} \\ 0 & \text{elsewhere.} \end{cases}\tag{3}$$

Further, in the momentum equation (2), the term h_{rmp} describes changes of the macroscopic local speed by assuming that on-ramp vehicles merge to the main road at speed $u_{rmp} < u$ and, conversely, that drivers reduce their speed to u_{rmp} before leaving the main road. Hence, this term is given as

$$h_{rmp}(x, t) = \frac{q \cdot r_{rmp}}{\rho} + \frac{(u_{rmp} - u)|q_{rmp}|}{l_{rmp}}.\tag{4}$$

5

We note that, usually, one assumes $u_{rmp} \approx u$ [15, 16].

In equation (2), $\theta = A(\rho)u^2$ is a pressure-like term, with $A(\rho)$ being a density-dependent variance factor given by the Fermi function as:

$$A(\rho) = A_0 + \delta A \left[1 + \tanh\left(\frac{\rho - \rho_{cr}}{\delta\rho}\right) \right]$$

in which ρ_{cr} is the critical density, which reflects the boundary between free flow and congested traffic, with A_0 and $A_0 + 2\delta A$ the variance prefactors between the two states; while $\delta\rho$ denotes the width of the transition region. Typical range of values for the constants $A_0, \delta A$ and $\delta\rho$ are given in Table 1, along with the typical range of the other parameters for this model following [44, 15, 16, 11, 30, 47, 7]. These parameters are meaningful, measurable, and have the correct order of magnitude for highway traffic while they can be adapted to city traffic as well [47].

The model also includes a traffic relaxation term aiming to keep flow in equilibrium, with $V_e^\star$ being the, non-local and dynamic, equilibrium speed (maximum out-of danger velocity meant to mimic drivers' behavior) with τ being a relaxation time. $V_e^\star(\rho, u, \rho_a, u_a)$ depends not only on the local density ρ and mean speed u, but also on the non-local density ρ_a and mean speed u_a, and is defined as

$$V_e^\star(\rho, u, \rho_a, u_a) = u_{\max}\left[1 - \frac{\theta + \theta_a}{2A(\rho_{\max})}\left(\frac{\rho_a T}{1 - \rho_a/\rho_{\max}}\right)^2 B(\delta u) \right]. \tag{5}$$

According to (5), $V_e^\star$ is given by the maximum velocity $u_{\max}$, reduced by a term that reflects necessary deceleration maneuvers. Both ρ_a and u_a are computed at an anticipated location $x_a = x + \gamma(1/\rho_{\max} + T \cdot u)$ with T being the desired time-gap and γ a scale factor. Finally, B is a so-called Boltzmann (interaction) factor, which, with $\delta u = \dfrac{u - u_a}{\sqrt{\theta + \theta_a}}$, is determined as

$$B(z) = 2\left[z\frac{e^{-z^2/2}}{\sqrt{2\pi}} + (1 + z^2)\int_{-\infty}^{z}\frac{e^{-y^2/2}}{\sqrt{2\pi}}dy \right].$$

This term contains the standard normal distribution and the Gaussian error function and describes the dependence of the braking interaction on the dimensionless velocity difference δu between the actual location x and the anticipation location x_a.

The crucial difference between the GKT model and other macroscopic traffic flow models is its non-local character. The non-local relaxation term in (5) has smoothing properties similar to those of a viscosity term, but its effect is forwardly directed and, therefore, more realistic. Furthermore, this non-local interaction term allows for fast and robust numerical integration, so that even extended freeway networks can be simulated in reasonable computational times. In contrast to other macroscopic models, the steady-state speed-density relation, $V^e(\rho)$, is not explicitly given,

Parameters	Units	Typical Values
Desired free speed, $u_{\max}$	km/h	$[110, 130]$
Maximum density, $\rho_{\max}$	veh/km	$[140, 160]$
Critical density, ρ_{cr}	veh/km	$[0.25, 0.4]\rho_{\max}$
Desired time gap, T	s	$[1, 2]$
Anticipation factor, γ		$[1, 2]$
Relaxation time, τ	s	$[20, 40]$
Variance pre-factor for free traffic, A_0		0.008
Pre-factor δA		$2.5A_0$
Transition width $\delta\rho$	veh/km	$[0.05, 0.1]\rho_{\max}$

Table 1: Typical range of the parameters used for the GKT traffic model (1)-(2)

but results from the steady-state on homogeneous roads (with no inflows our outflows) as

$$V^e(\rho) = \frac{\tilde{u}^2}{2u_{\max}}\left(-1 + \sqrt{1 + \frac{4u_{\max}^2}{\tilde{u}^2}}\right) \tag{6}$$

with the abbreviation

$$\tilde{u} = \frac{1}{T}\left(\frac{1}{\rho} - \frac{1}{\rho_{\max}}\right)\sqrt{\frac{A(\rho_{\max})}{A(\rho)}}.$$

This also determines the equilibrium traffic flow (the so-called fundamental diagram) $q^e(\rho) = \rho V^e(\rho)$, as shown in Fig. 1 for a standard parameter set.

Next, two approaches are presented to incorporate the modeling and effects of ACC and CACC mechanisms in the GKT model. This is done through the terms $\alpha\mathcal{V}_{acc}$ and $[1 - \beta F(\rho)]$ in equation (2), with $\alpha = 1$ for both approaches. The first approach is that presented in [32] obtained by setting $\beta = 0$; and the second is a novel one proposed in the present work obtained by setting $\beta = 1$. We emphasize here that, in the proposed approach, the original GKT non-local interaction term is smoothly switched off and replaced by a new term $\mathcal{V}_{acc}$ by a Fermi-like function $F(\rho)$ such that in congested traffic flow the new term takes over.

Ngoduy's [32] ACC & CACC approach. In [32] a macroscopic model for ACC and CACC traffic flow dynamics was derived and studied in the framework of the GKT model presented above. The proposed cooperative mechanism lies in the fact that the equipment in ACC vehicles makes the car-following behavior more responsive and agile, with respect to the leading vehicle (with increased multi-anticipation for CACC), especially in congested situations, by getting an extra interaction through exogenous factors of the intelligent devices. The main idea is to represent the instantaneous response of the ACC (and CACC) system due to changes of the speed of the leading
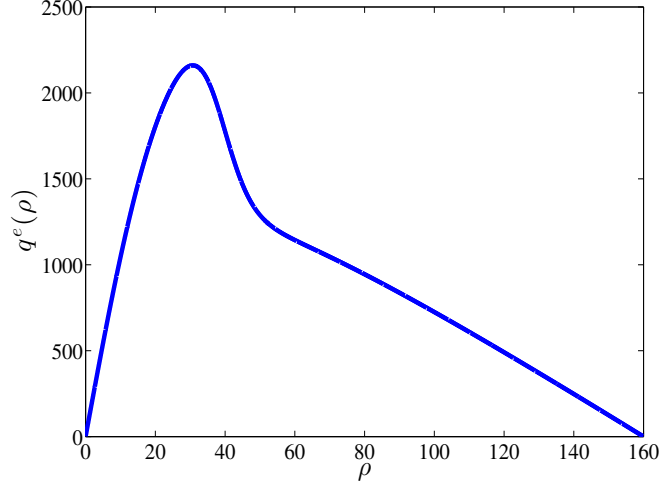
Figure 1: Equilibrium flow-density diagram of the GKT model for $u_{\max} = 110$ km/h, $\rho_{\max} = 160$ veh/km, $T = 1.8s$

vehicle(s) by deducing an acceleration/deceleration term in (2), which reads as

$$\mathcal{V}_{acc}(\rho, u) = \frac{\partial u}{\partial x} \sum_{m=1}^{M} \frac{m}{\tau_m^{\star}}, \tag{7}$$

with M being the number of preceding vehicles that the follower could exchange information (interact) with, while $M = 1$ corresponds to an ACC system. The, density dependent, sensitivity coefficients $\tau_m^{\star}$ are constructed so that the CACC equipment revert to normal speed control in free-flow situations, that is

$$\frac{1}{\tau_m^{\star}} = \frac{1}{2\tau_m^0} \left[1 + \tanh\left(\frac{\rho - \rho_{cr}}{\Delta \rho}\right) \right], \tag{8}$$

where τ_m^0 reflects the relaxation time of the CACC vehicle to the mth leader in a congested traffic situation. Under the assumption that a CACC vehicle takes longer time to relax to the furthest Mth leader, it is supposed that $\tau_1^{\star} < \tau_2^{\star} < \cdots < \tau_M^{\star}$ and that $\sum_{m=1}^{M} \frac{1}{\tau_m^{\star}} = \frac{1}{\tau^{\star}}$, where $\tau^{\star}$ is the relaxation time of the ACC system.

Typical values proposed in [32], and also adopted in the present work, are $M = 1$ and $\tau^0 = 1s$ for the ACC system and $M = 3$ and $[\tau_1^0, \tau_2^0, \tau_3^0] = [2, 3, 6]s$ for the CACC one. Further, the transition width in (8), $\Delta\rho$, was set equal to $0.1\rho_{\max}$, and the behavior of this choice with respect to density is depicted in Fig. 2.

A new approach to ACC & CACC. Here a novel approach to modeling ACC and CACC effects in the GKT model is presented. One major difference between this new approach and that from [32] is that the ACC/CACC term in the previously presented model contributes to the so-called convection term in the momentum equation; whereas in our approach the corresponding term contributes to the non-local relaxation term in the GKT model equations. Moreover, in our ACC and CACC modeling approach the time-gap parameter, which is an important characteristic of such systems, will be explicitly taken into account. The ability to explicitly define the time-gap in our approach enables the model to simulate ACC/CACC flows with different time-gap settings, which lead to different dynamic behavior and equilibrium capacities. This ability also gives the opportunity to assess the impact of the time-gap settings on traffic flow performance.

We derive our approach on the basis of the control objectives that an ACC system should follow, in accordance to [42]:

I. To travel with the maximum speed, set by the driver, in cases where no leading vehicles exist in the range covered by the sensors, or leading vehicles exist within range but their velocities are higher than the maximum speed set by the user (*speed control mode*).

II. To maintain vehicle speed equal to the speed of the leading vehicle at a specified distance, when the leading vehicle is in range and its speed is lower than the maximum speed set by the driver (*gap control mode*).

III. Transitions between the two aforementioned objectives should be as smooth as possible, in order not to cause discomfort to the passengers, due to abrupt accelerations or decelerations.

Before we proceed, to avoid confusion, we need to clarify the terms *headway* and *time-gap*. *Time/space-headway* is the time/space distance between the front bumper of the preceding vehicle and the front bumper of the following vehicle, while *time/space-gap* is the time/space distance between the rear bumper of the preceding vehicle and the front bumper of the following one. In a Constant Time Headway (CTH) policy the inter-vehicle spacing is a linear function of the vehicle's speed, which feels more natural to the passengers of the ACC equipped vehicle. This type of ACC (and - in extension - CACC) policy was adopted for the proposed model in this work.

To satisfy the above objectives, the proposed model is based on the following assumptions: (1) For densities clearly below a threshold ρ_{acc} (being lower than or equal to ρ_{cr}) the additional term to the GKT has no effect, as it is supposed that (on average) the drivers set their maximum speeds (or react) as in a manual manner, i.e. as the GKT model describes (emulating in that way the speed control mode). In the region around ρ_{acc}, a smooth but fast transition between the previous case and the ACC/CACC-controlled situation takes place, described using again the Fermi function:

$$F(\rho) = \frac{1}{2}\left[1 + \tanh\left(\frac{\rho - \rho_{acc}}{\Delta\rho}\right)\right]. \tag{9}$$

In our model, to achieve this fast transition, the transition width $\Delta\rho$ takes much lower values, of $\Delta\rho = 0.025\rho_{max}$, compared to those in Ngoduy's model, leading to much steeper transition between the two states. We refer to Fig. 2 for a comparison.

9
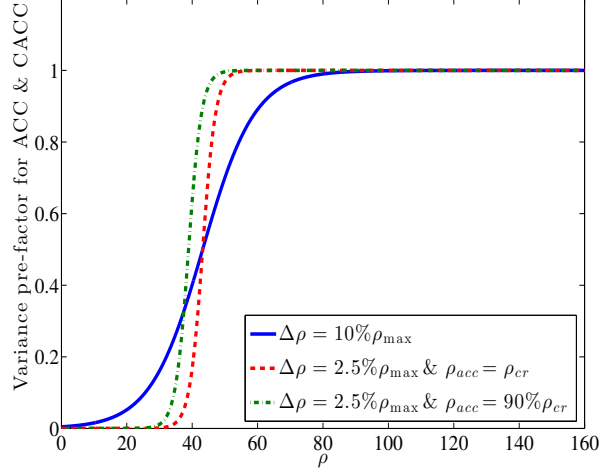
Figure 2: Variance factor $\frac{1}{2}\left[1 + \tanh\left(\frac{\rho-\rho_{acc}}{\Delta\rho}\right)\right]$ for $\rho_{\max} = 160$ veh/km and $\rho_{cr} = 0.27\rho_{\max}$

(2) During the gap control mode, a constant time gap $T^\star$ is desired, which is imposed through its corresponding effect on a desired density $\rho^\star$ as

$$\rho^\star = \frac{1}{1/\rho_{\max} + T^\star u^\star}, \tag{10}$$

where the denominator is the desired space headway, with $1/\rho_{\max}$ reflecting the vehicle length and $u^\star = u(x^\star)$ is the speed of the preceding vehicle, computed at position

$$x^\star = x + \gamma^\star(1/\rho_{\max} + T^\star \cdot u), \quad \gamma^\star \in [1, 2].$$

Additionally, the desired speed relaxes to the speed of the preceding vehicle $u^\star$ after a relaxation time $\tau^\star$. As a result, the corresponding source term can be modeled for ACC vehicles as:

$$\mathcal{V}_{acc}(\rho, u, \rho^\star, u^\star) = \frac{1}{2}\left[1 + \tanh\left(\frac{\rho - \rho_{acc}}{\Delta\rho}\right)\right]\left(\frac{\rho^\star u^\star - \rho u}{\tau^\star}\right) \tag{11}$$

In [27] it was demonstrated that the minimum time-gap that can be achieved by ACC vehicles is $0.8s$. In general, indicative values used for ACC traffic are $T^\star \in [0.8, 2.2]s$, following [ISO 15622,2010] standards, and $\tau^\star \approx 1s$.

For CACC vehicles a similar approach is used, but the corresponding source term takes into account the speeds of more than one preceding vehicles, with a different time relaxation for each one of them. The ability for the system to look downstream increases the smoothing effect of the corresponding source term. Furthermore, this additional information from far downstream allows

for the use of lower values of time gaps (without compromising safety), which was also used in the present study. For example, in [49], it was identified that CACC vehicles enable closer vehicle following, with time-gap as low as 0.5 s. However, such a time gap is too short to be controllable by humans, as for the stat-of-the-art ACC systems, the driver is required to be able to take over at any time; consequently this requires the next step of ITS, autonomous driving. As reduced time gaps are only achievable between vehicles that are equipped with the CACC technology the market penetration rate for these systems plays an important role as well. In [49] it was concluded that the CACC technology has the potential to increase significantly the highway capacity, even doubling it if the penetration rate is high.

Thus, we propose for CACC traffic

$$\mathcal{V}_{acc}(\rho, u, \rho^\star, u^\star) = \frac{1}{2}\left[1 + \tanh\left(\frac{\rho - \rho_{acc}}{\Delta\rho}\right)\right]\sum_{i=1}^{M}\left(\frac{\rho^\star u_i^\star - \rho u}{\tau_i^\star}\right) \tag{12}$$

where $u_i^\star = u(x_i^\star)$ with $x_i^\star = x + i \cdot \gamma^\star(1/\rho_{\max} + T^\star \cdot u)$, $\quad i = 1, \ldots, M$, and

$$\rho^\star = \frac{1}{1/\rho_{\max} + T^\star u_1^\star}.$$

The parameter values used in this work for CACC traffic are $M = 3$ with $[\tau_1^\star, \tau_2^\star, \tau_3^\star] = [2, 3, 6]$ as to be consistent with the values used in [32].

In summary, the first approach for ACC/CACC traffic, from [32], contributes essentially to the convection term, by introducing an acceleration/deceleration term in the flow equation, while the new approach contributes to the relaxation term of the GKT model.

Remark 1. *The incorporation of the ACC/CACC terms in equation (2) using the parameters α and β can provide a further generalization of the model in terms of the assumed penetration rate, p, of ACC/CACC-equipped vehicles in the flow. Although, in this work a penetration rate of $p = 1$ is assumed, as stated in the Introduction, flows with penetration rates lower than 1 maybe simulated by appropriately modifying the values of the parameters α and β by setting them equal to p. This approach is based on the observation that in some situations, the macroscopic dynamics of microscopic models with heterogeneous vehicles/drivers is essentially that of identical vehicles/drivers with parameters equal to the mean of the heterogeneous vehicle/driver population. This approach will be investigated in future work.*

3. The relaxation approach and its numerical discretization

Model equations (1)-(2) can be written in vector form, supplied with initial conditions, as

$$\partial_t \mathbf{u} + \partial_x \mathbf{f}(\mathbf{u}) = \mathbf{s}(\mathbf{u}),$$
$$\mathbf{u}(x, 0) = \mathbf{u}_0(x), \tag{13}$$

11

where the functions $\mathbf{u}$, $\mathbf{f(u)}$ and $\mathbf{s(u)} \in \mathbb{R}^2$ with $\mathbf{u} = [\rho,\ q]^T$, $\mathbf{f(u)} = [\rho u,\ \rho u^2 + \theta \rho]^T$ and $\mathbf{s(u)} = [r_{rmp},\ (1 - \beta F(\rho))(\rho V_e^\star(\rho, u, \rho_a, u_a) - \rho u)/\tau + h_{rmp} + \alpha \mathcal{V}_{acc}]^T$. Systems in the form of (13) can be rewritten in quasi-linear form

$$\partial_t \mathbf{u} + \mathbf{J(u)}\partial_x \mathbf{u} = \mathbf{s(u)}, \tag{14}$$

where $\mathbf{J(u)} = \dfrac{\partial \mathbf{f}}{\partial \mathbf{u}}$ is the Jacobian matrix of the system, given as

$$\mathbf{J(u)} = \begin{bmatrix} 0 & 1 \\ \dfrac{\partial P}{\partial \rho} - u^2 & \dfrac{\partial P}{\partial q} + 2u \end{bmatrix}, \quad \text{with } P = \rho\theta(\rho, u). \tag{15}$$

The Jacobian matrix has two distinct and real (positive) eigenvalues, for all physically reasonable parameter sets, given as

$$\lambda_{1,2} = u + \frac{1}{2}\frac{\partial P}{\partial q} \pm \sqrt{\left(\frac{1}{2}\frac{\partial P}{\partial q}\right)^2 + \frac{q}{r}\frac{\partial P}{\partial q} + \frac{\partial P}{\partial \rho}} = u\left(1 + A(\rho) \pm \sqrt{A(\rho)^2 + A(\rho) + \rho\frac{dA(\rho)}{d\rho}}\right), \tag{16}$$

which denote that the model equations constitute a strictly hyperbolic set of partial differential equations.

3.1. The relaxation model

In this section we briefly present the class of relaxation models introduced in [24] and applied in various second-order macroscopic traffic flow models in [7]. By the introduction of the artificial, relaxation, variables $\mathbf{v}$ the relaxation system, corresponding to (13), reads as

$$\partial_t \mathbf{u} + \partial_x \mathbf{v} = \mathbf{s(u)},$$
$$\partial_t \mathbf{v} + \mathbf{C}^2 \partial_x \mathbf{u} = \frac{\mathbf{f(u)} - \mathbf{v}}{\epsilon}, \tag{17}$$

with initial data

$$\mathbf{u}(x, 0) = \mathbf{u}_0(x),$$
$$\mathbf{v}(x, 0) = \mathbf{v}_0(x) = \mathbf{f}(\mathbf{u}_0(x)),$$

where the small parameter ϵ ($0 < \epsilon \ll 1$), is the *relaxation rate* and $\mathbf{C}^2 = \text{diag}\{c_1^2, c_2^2\}$ is a positive diagonal.

For small ϵ, and applying the Chapman-Enskog expansion in system (17), see for example [24, 28], the following approximation for $\mathbf{u}$ can be obtained,

$$\partial_t \mathbf{u} + \partial_x \mathbf{f(u)} = \mathbf{s(u)} + \epsilon\partial_x\left[\left(\frac{\partial \mathbf{f(u)}}{\partial \mathbf{u}}\right)\mathbf{s(u)}\right] + \epsilon\partial_x\left[\left(\mathbf{C}^2 - \left(\frac{\partial \mathbf{f(u)}}{\partial \mathbf{u}}\right)^2\right)\partial_x \mathbf{u}\right] + O(\epsilon^2). \tag{18}$$

Equation (18) controls the first-order behavior of system (17), with the third term on the right-hand

side being an $O(\epsilon)$ dominant dissipation term in the model and $\left(\mathbf{C}^2 - \left(\frac{\partial \mathbf{f}(\mathbf{u})}{\partial \mathbf{u}}\right)^2\right)$ being the diffusion-like coefficient matrix. The model (17) is well-posed only if this matrix is positive semi-definite for all $\mathbf{u}$. This requirement on the diffusion coefficient matrix is the well-known *sub-characteristic condition*, [26, 24], i.e.

$$\mathbf{C}^2 - \left(\frac{\partial \mathbf{f}(\mathbf{u})}{\partial \mathbf{u}}\right)^2 \geq 0, \quad \forall \mathbf{u}, \tag{19}$$

which ensures the dissipative nature of (18); and it is equivalent to

$$\lambda^2 \leq c^2, \quad \text{where} \quad \lambda = \max_{1 \leq i \leq 2} |\lambda_i| \quad \text{and} \quad c = \min_{1 \leq i \leq 2} |c_i|. \tag{20}$$

Condition (19) can always be satisfied by choosing sufficiently large values for the diagonal elements in $\mathbf{C}^2$, for $\mathbf{u}$ varying in a bounded domain. As such, the solution of the relaxation model (17) converges strongly to the unique entropy solution of the original conservation laws [6, 28].

System (17) can be easily diagonalized leading to the following decoupled system of equations:

$$\partial_t(\mathbf{v} + \mathbf{C}\mathbf{u}) + \mathbf{C}\partial_x(\mathbf{v} + \mathbf{C}\mathbf{u}) = \frac{\mathbf{f}(\mathbf{u}) - \mathbf{v}}{\epsilon} + \mathbf{C}\mathbf{s}(\mathbf{u}); \tag{21}$$

$$\partial_t(\mathbf{v} - \mathbf{C}\mathbf{u}) - \mathbf{C}\partial_x(\mathbf{v} - \mathbf{C}\mathbf{u}) = \frac{\mathbf{f}(\mathbf{u}) - \mathbf{v}}{\epsilon} - \mathbf{C}\mathbf{s}(\mathbf{u}). \tag{22}$$

The left-hand side of system (21)-(22) is linear with constant wave speeds, split into positive and negative parts. Thus, its solution has the property that it propagates at finite speeds along linear characteristic curves $dx/dt = \pm\mathbf{C}$. From (21)-(22) and by setting $\mathbf{g}_{1,2} = \mathbf{v} \pm \mathbf{C}\mathbf{u}$, the follow relations can be obtained that recover the original variables of the relaxation system,

$$\mathbf{u} = \frac{1}{2}\mathbf{C}^{-1}(\mathbf{g}_1 - \mathbf{g}_2) \quad \text{and} \quad \mathbf{v} = \frac{1}{2}(\mathbf{g}_1 + \mathbf{g}_2). \tag{23}$$

The structure of the linear characteristic field of the relaxation system constitutes a clear advantage compared to the original conservation laws for their numerical integration.

3.2. Discretizations in space and time

Let $x_i = i\Delta x$, $x_{i\pm\frac{1}{2}} = (i \pm \frac{1}{2})\Delta x$, where Δx is a uniform spatial discretization step. The discrete cell average of $\mathbf{u}$ in the cell $I_i = [x_{i-\frac{1}{2}}, x_{i+\frac{1}{2}}]$ at time t is defined as $\mathbf{u}_i(t)$, i.e. $\mathbf{u}_i(t) = \frac{1}{\Delta x}\int_{I_i} \mathbf{u}(x,t)dx$, and the approximate value of $\mathbf{u}$ at $(x_{i+\frac{1}{2}}, t)$ by $\mathbf{u}_{i+\frac{1}{2}}(t)$. Integrating (17), for continuous time, the semi-discrete relaxation system is given as

$$\begin{aligned} \frac{\partial}{\partial t}\mathbf{u}_i + \frac{1}{\Delta x}\left(\mathbf{v}_{i+\frac{1}{2}} - \mathbf{v}_{i-\frac{1}{2}}\right) &= \mathbf{s}(\mathbf{u})_i, \\ \frac{\partial}{\partial t}\mathbf{v}_i + \frac{\mathbf{C}^2}{\Delta x}\left(\mathbf{u}_{i+\frac{1}{2}} - \mathbf{u}_{i-\frac{1}{2}}\right) &= -\frac{1}{\epsilon}(\mathbf{v}_i - \mathbf{f}(\mathbf{u})_i). \end{aligned} \tag{24}$$

13

where $\mathbf{s}(\mathbf{u})_i$ and $\mathbf{f}(\mathbf{u})_i$ are discrete averages of the source term and flux function, respectively. To completely define the spatial discretization, we need to compute the flux values $\mathbf{u}_{i\pm\frac{1}{2}}$ and $\mathbf{v}_{i\pm\frac{1}{2}}$.

As system (17) has linear characteristics and its characteristic speeds, $+c_k$ and $-c_k$, are constant, the construction of an upwind scheme is much simpler than developing such a scheme for the original nonlinear conservation laws. For example, the *first-order upwind* scheme, [24, 39, 7], applied to $\mathbf{g}_1$ and $\mathbf{g}_2$ gives $\mathbf{g}_{1_{i+\frac{1}{2}}} = \mathbf{g}_{1_i}$ and $\mathbf{g}_{2_{i+\frac{1}{2}}} = \mathbf{g}_{2_{i+1}}$.

To increase the spatial order of accuracy, a WENO-type interpolant approach is applied, where the approximate solution is reconstructed using higher-order polynomials. By direct application of this reconstruction to the $k-$th components of the characteristic variables, $\mathbf{g}_{1,2} = \mathbf{v} \pm \mathbf{Cu}$, a non-oscillatory higher-order spatial discretization is obtained. The superiority of applying higher-order schemes, compared to low-order ones, in traffic flow simulations has been recently demonstrated in [7]. By applying the fifth-order WENO reconstruction proposed in [5], the discrete values of each component of $\mathbf{g}_{1_{i+\frac{1}{2}}}$ and $\mathbf{g}_{2_{i+\frac{1}{2}}}$, at a cell boundary $i + \frac{1}{2}$, are defined as left and right extrapolated values $\mathbf{g}^L_{1_{i+\frac{1}{2}}}$ and $\mathbf{g}^R_{2_{i+\frac{1}{2}}}$ i.e.

$$\mathbf{g}_{1_{i+\frac{1}{2}}} = \mathbf{g}^L_{1_{i+\frac{1}{2}}} \quad \text{and} \quad \mathbf{g}_{2_{i+\frac{1}{2}}} = \mathbf{g}^R_{2_{i+\frac{1}{2}}}. \tag{25}$$

For a general function $\psi(x)$ the *fifth-order accurate* extrapolated value $\psi^L_{i+\frac{1}{2}}$ is defined as

$$\psi^L_{i+\frac{1}{2}} = \sum_{r=0}^{2} \omega^-_r h^-_r \tag{26}$$

where h^-_r are extrapolated values obtained from cell averages in the rth stencil $(i-r, i-r+1, i-r+2)$ as

$$h^-_0 = \frac{1}{3}\psi_i + \frac{5}{6}\psi_{i+1} - \frac{1}{6}\psi_{i+2};$$

$$h^-_1 = -\frac{1}{6}\psi_{i-1} + \frac{5}{6}\psi_i + \frac{1}{3}\psi_{i+1};$$

$$h^-_2 = \frac{1}{3}\psi_{i-2} - \frac{7}{6}\psi_{i-1} + \frac{11}{6}\psi_i,$$

and $\omega^-_r, r = 0, 1, 2$ are non-linear WENO weights given by

$$\omega^-_r = \frac{a_r}{\sum_{l=0}^{2} a_l}, \quad a_r = C_r\left(1 + \frac{\eta_5}{IS^-_r + \varepsilon}\right), \quad r = 0, 1, 2 \tag{27}$$

with $C_0 = 3/10, C_1 = 3/5, C_2 = 1/10$, and ε being a very small number used to assure that the denominator does not vanish; in our numerical implementation is set to $\varepsilon = 10^{-40}$, as suggested in

14

[5]. The smoothness indicators IS_r^- are given by

$$
\begin{aligned}
IS_0^- &= \frac{13}{12}(\psi_i - 2\psi_{i+1} + \psi_{i+2})^2 + \frac{1}{4}(3\psi_i - 4\psi_{i+1} + \psi_{i+2})^2; \\
IS_1^- &= \frac{13}{12}(\psi_{i-1} - 2\psi_i + \psi_{i+1})^2 + \frac{1}{4}(\psi_{i-1} - \psi_{i+1})^2; \\
IS_2^- &= \frac{13}{12}(\psi_{i-2} - 2\psi_{i-1} + \psi_i)^2 + \frac{1}{4}(\psi_{i-2} - 4\psi_{i-1} + 3\psi_i)^2.
\end{aligned}
$$

The expression η_5 is given in terms of the smoothness indicators as

$$
\eta_5 = |IS_0^- - IS_2^-|.
$$

For the right face value $\psi_{i+\frac{1}{2}}^R$, the corresponding weights ω_r^+ and smoothness indicators are given by symmetry. After the above reconstructions have been performed to each component of the characteristic variables from (25), the numerical fluxes for $\mathbf{u}_{i\pm\frac{1}{2}}$ and $\mathbf{v}_{i\pm\frac{1}{2}}$ are computed from (23). In a similar manner we compute the face values at cell boundary $i - \frac{1}{2}$.

Source term's discretization. The discrete average values in (24) for the flux function, $\mathbf{f(u)}_i$, and source term, $\mathbf{s(u)}_i$, can be obtained by using high-order quadrature rules, such as Simpson's rule. However, for small values of the relaxation rate ϵ it is sufficient to project $\mathbf{f(u)}_i$ and $\mathbf{s(u)}_i$ into the local limit values $\mathbf{f}(\mathbf{u}_i)$ and $\mathbf{s}(\mathbf{u}_i)$, respectively [38, 39].

In addition, for every computational cell $I_i = [x_{i-\frac{1}{2}}, x_{i+\frac{1}{2}}]$ and at each time step, we have to compute the non-local values ρ_a and u_a in (5) at the anticipated location x_a. As generally the position of x_a is not a multiple of Δx, we implement the following procedure to define the computational cell x_a belongs to, for computing ρ_a and u_a. As $x_i = (i-1)\Delta x$, we can locate the cell $I_k, k = i, i+1, \ldots$, in which x_a belongs with $k = i + \lfloor \frac{x_a - (x_i - 0.5\Delta x)}{\Delta x} \rfloor$, where $\lfloor \cdot \rfloor$ is the floor function. Then, in the cell I_k a piecewise linear interpolation is performed, using the high-order reconstructed values at the right and left of the cell faces $x_{k-\frac{1}{2}}$ and $x_{k+\frac{1}{2}}$, respectively. For example, $(\rho_a)_i$ is computed as

$$
(\rho_a)_i = \rho_{k-\frac{1}{2}}^R + \frac{\rho_{k+\frac{1}{2}}^L - \rho_{k-\frac{1}{2}}^R}{\Delta x}\left(x_a - x_{k-\frac{1}{2}}\right).
$$

A similar procedure was also proposed in [47]. With the same procedure we compute the non-local terms for the ACC and CACC modeling from (11) and (12), respectively, while for the velocity derivative approximation in (7) a fourth-order finite difference approximation was implemented.

3.3. Time integration

The semi-discrete relaxation system (24) constitutes a system of autonomous ordinary differential equations which can be formulated as

$$
\frac{d\mathcal{Y}}{dt} = \mathcal{F}(\mathcal{Y}) - \frac{1}{\epsilon}\mathcal{G}(\mathcal{Y}), \tag{28}
$$

with the time-dependent vector functions given as

$$\mathcal{Y} = \begin{pmatrix} \mathbf{u}_i \\ \mathbf{v}_i \end{pmatrix}, \quad \mathcal{F}(\mathcal{Y}) = \begin{pmatrix} \mathbf{s(u)}_i - \Delta_i \mathbf{v}_i \\ -\mathbf{C}^2 \Delta_i \mathbf{u}_i \end{pmatrix} \quad \text{and} \quad \mathcal{G}(\mathcal{Y}) = \begin{pmatrix} 0 \\ \mathbf{v}_i - \mathbf{f(u)}_i \end{pmatrix},$$

with

$$\Delta_i \mathbf{v}_i = \frac{\mathbf{v}_{i+\frac{1}{2}} - \mathbf{v}_{i-\frac{1}{2}}}{\Delta x} \quad \text{and} \quad \Delta_i \mathbf{u}_i = \frac{\mathbf{u}_{i+\frac{1}{2}} - \mathbf{u}_{i-\frac{1}{2}}}{\Delta x}.$$

A time marching approach based on implicit-explicit (IMEX) Runge-Kutta (RK) splitting for (28) is considered as to avoid the time step restrictions imposed by an explicit solver due to stiffness. As such, the explicit RK scheme treats the non-stiff stage of the splitting for $\mathcal{F}(\mathcal{Y})$ while a diagonally implicit RK scheme treats the stiff stage for $\mathcal{G}(\mathcal{Y})$ [3, 37, 38, 39, 40?]. We note that even though an implicit scheme is used, either linear or nonlinear algebraic equations have to be solved due to the special structure of the relaxation system.

Defining as Δt^n the current time step and $\mathcal{Y}^n$ the approximate solution at $t = t_n$, the $s-$stage IMEX method can be implemented as

$$\mathcal{Y}_k = \mathcal{Y}^n + \Delta t^n \sum_{m=1}^{k-1} \tilde{a}_{km} \mathcal{F}(\mathcal{Y}_m) - \frac{\Delta t^n}{\epsilon} \sum_{m=1}^{s} a_{km} \mathcal{G}(\mathcal{Y}_m), \quad k = 1, 2, \ldots, s \tag{29}$$

$$\mathcal{Y}^{n+1} = \mathcal{Y}^n + \Delta t^n \sum_{k=1}^{s} \tilde{b}_k \mathcal{F}(\mathcal{Y}_k) - \frac{\Delta t^n}{\epsilon} \sum_{k=1}^{s} b_k \mathcal{G}(\mathcal{Y}_k). \tag{30}$$

The $s \times s$ matrices $\tilde{\mathbf{A}} = [\tilde{a}_{km}]$ and $\tilde{\mathbf{A}} = [a_{km}]$ are chosen such that the splitting is explicit in $\mathcal{F}(\mathcal{Y})$ and implicit in $\mathcal{G}(\mathcal{Y})$. The $s-$vectors $\tilde{\mathbf{b}}$ and $\mathbf{b}$ are the coefficients which characterize the IMEX scheme [37] and are given in a double tableau as

$$\begin{array}{c|c} \tilde{\mathbf{d}} & \tilde{\mathbf{A}} \\ \hline & \tilde{\mathbf{b}}^{\mathrm{T}} \end{array} \quad \text{and} \quad \begin{array}{c|c} \mathbf{d} & \mathbf{A} \\ \hline & \mathbf{b}^{\mathrm{T}} \end{array}$$

where $\tilde{\mathbf{d}}$ and $\mathbf{d}$ are the $s-$vectors used in the context of non-autonomous systems of differential equations. The left and right tables are associated with the explicit and implicit RK schemes, respectively. Here we implement the *third-order IMEX method* from [3] where its double tableau is given as

0	0	0	0		0	0	0	0
γ	γ	0	0		γ	0	γ	0
$1-\gamma$	γ-1	$2-2\gamma$	0	and	$1-\gamma$	0	$1-2\gamma$	γ
	0	$\frac{1}{2}$	$\frac{1}{2}$			0	$\frac{1}{2}$	$\frac{1}{2}$

with $\gamma = (3 + \sqrt{3})/6$. Using this IMEX scheme, the source terms are treated implicitly and the advection terms are treated explicitly and the high-order relaxation scheme is stable independently

of ϵ. Thus, the choice of Δt^n in each time step is based only on a usual CFL condition [24],

$$CFL = \max\left((\max_{i,k} c_k^n)\frac{\Delta t^n}{\Delta x}, \frac{\Delta t^n}{\Delta x}\right) \leq \frac{1}{2},$$

where the values of the relaxation constants c_k^n are re-computed at each time step.

The relaxation constants c_k^n in $\mathbf{C}^2$ should satisfy criterion (19) and the size of $\mathbf{C}^2$ influences the numerical dissipation of the numerical scheme. Larger c_k values usually add more numerical dissipation, thus for accuracy reasons it is desirable to have c_k as small as possible. The choice of their value can be based on rough estimates of the characteristic speeds of the original problem. For example, one can set every eigenvalue λ of $\mathbf{J}(\mathbf{u})$ to satisfy $|\lambda| \leq c_{\max}$, where $c_{\max} = \max_k c_k$. By doing so, we ensure that the characteristic speeds of the hyperbolic part of (17) are at least as large as the characteristic speeds of the original problem.

In our implementation, the values of $c_k^n, k = 1, 2$, are adjusted according to the behavior of the solution by considering a global selection on every time step Δt^n. Based on the global maximum of each eigenvalue of the system's Jacobian matrices over the grid cells I_i, their choice is made as

$$c_k^n = \max_i |\lambda_k^n| + e, \ \ k = 1, 2,$$

where e is a small correction parameter of $O(10^{-2})$, added to avoid the characteristic speeds from vanishing. The above choice was found sufficient for our simulations in the next sections.

3.4. Initial and boundary conditions

Initial and boundary condition for the relaxation system are imposed for the relaxation variables keeping in mind that at the small relaxation limit, $\epsilon \to 0^+$, the equilibrium $\mathbf{v} = \mathbf{f}(\mathbf{u})$ should be satisfied. Following from that for a given initial condition $\mathbf{u}(x, 0) = \mathbf{u}_0(x)$ we set $\mathbf{v}(x, 0) = \mathbf{v}_0(x) \equiv \mathbf{f}(\mathbf{u}_0(x))$, thus satisfying the local equilibrium and avoid the introduction of an initial layer from the relaxation system. In a similar way different boundary conditions can be imposed to the relaxation system, e.g. periodic, Dirichlet or homogeneous Neumann, thus avoiding the introduction of artificial boundary layers. We refer to [7] for more details on this subject.

4. Numerical simulations and discussion

In this section, we extensively investigate numerically the performance of the models presented, which aim to describe the traffic flow dynamics for the different vehicle types such as, manually driven, ACC and CACC vehicles. We consider two main categories of test cases in the numerical simulations. The first one is for traffic flows on a circular homogeneous freeway where we aim to examine the formation of traffic instabilities and the general flow characteristics with respect to small and large perturbations introduced in the flow field. The potential stabilization effects on the traffic flow when ACC or CACC vehicles are considered is of primary importance. The second category of test cases is the simulation of a freeway with an on-ramp i.e. a potential bottleneck.

Different traffic states (i.e. congestion patterns) can be developed close to the bottleneck caused by the on-ramp. Here we aim to investigate the different states that occur from the on-ramp flow and to determine if the proposed ACC and CACC approaches can act as a sort of control measures to avoid the different resulting breakdowns of traffic. We note here that, for brevity, the above mentioned test cases are chosen as to highlight the difference of the two implemented ACC and CACC approaches and to give a clear insight to their performance. However, further validation of the proposed model, including comparisons with microscopic simulations, constitutes an ongoing work which will be presented in the future. For all numerical tests presented next, the relaxation rate ϵ was set to 10^{-8} and the CFL value to 0.4.

4.1. Homogeneous Traffic with Localized Perturbations

In the tests presented in this section, we assume that the traffic flow is in a ring of circumference of $L = 10km$, thus periodic boundary conditions were implemented. Following [44, 15, 16, 7], we consider a dipole-like initial variation of the average density $\bar{\rho}$, as shown in Fig. 3, given as

$$\rho(x,0) = \bar{\rho} + \Delta\rho \left[\cosh^{-2}\left(\frac{x - x_0}{w^+}\right) - \frac{w^+}{w^-} \cosh^{-2}\left(\frac{x - x_0 - \Delta x_0}{w^-}\right) \right]$$

where $w^+ = 201.5$ and $w^- = 805m$ with $\Delta x_0 = w^+ + w^-$. The initial flow $q(x,0) = q_e(\rho(x,0)) = \rho V^e(\rho)$, and following from (6), is assumed in local equilibrium. The induced perturbation eventually leads to instabilities for given values of $\bar{\rho}$. This can be understood also intuitively, at larger densities a higher percentage of drivers that approach a density peak must brake, thus increasing the density peak. Depending on increased values of $\bar{\rho}$, different situations emerge. Starting with almost homogeneous initial traffic, the development of traffic instabilities consists a strict test also for numerical performance. Various tests were performed for different densities $\bar{\rho}$. The ring was discretized with $npts = 400$ grid points ($\Delta x = 25m$). The model parameters used in the simulations were $u_{\max} = 110$ km/h, $\rho_{max} = 160$ veh/km, $\rho_{cr} = 0.27\rho_{max}$, $\tau = 35s$, $A_0 = 0.008$, $\delta A = 0.02$, $\delta\rho = 0.1\rho_{max}$, $T = 1.8s$ and $\gamma = 1.2$. Simulations are reported up to final time of $1200s$.

Localized cluster. In the first scenario, $\bar{\rho} = 25$ and the initial perturbation was set to $\Delta\rho = 6$ veh/km. This traffic flow field is unstable, thus, by introducing the perturbation, a single density cluster is formed for manually driven cars, i.e. using the original GKT model, as shown in Fig. 3. As it can be seen, the perturbation first travels downstream and grows in its amplitude; and when it gets large enough, it starts propagating upstream. Next, and in Fig. 4, the results for the evolution of density for ACC and CACC traffic flows using model (7), with the coefficient $\tau^0 = 1s$ for ACC and the CACC coefficients $[\tau_1^0, \tau_2^0, \tau_3^0] = [2, 3, 6]s$, as proposed in [32], are shown. For ACC traffic flow, a stable flow field of uncongested traffic is obtained, with the initial perturbation traveling downstream; while for CACC cars the initial perturbation dies out with time. In Fig. 5 the obtained profiles of density, speed and flow rate at $t = 1200s$ are shown for manual, ACC and CACC traffic. The resulted uncongested traffic can be clearly seen along with an increased traffic flow rate along the total length of the ring road.

18
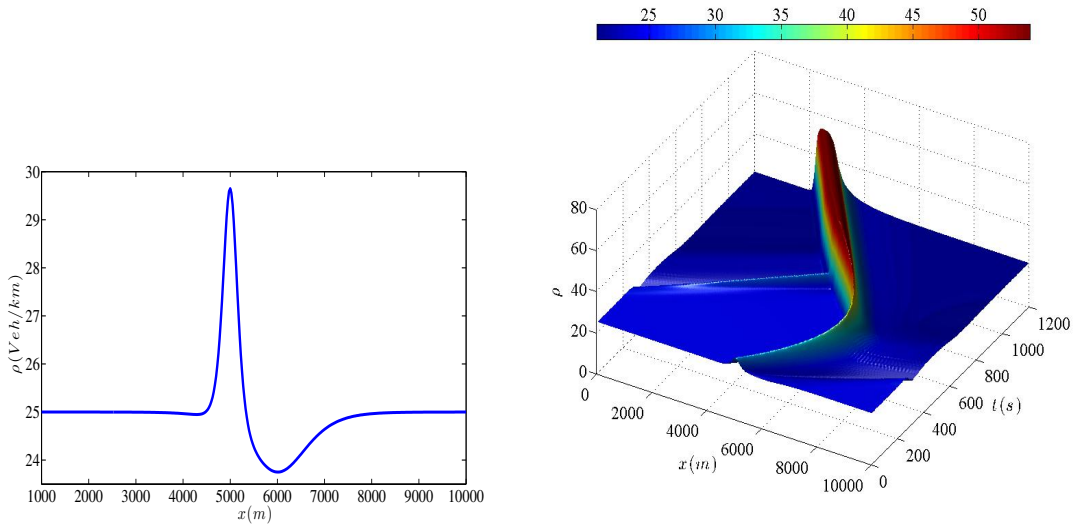
Figure 3: Initial perturbation for $\bar{\rho} = 25$ and $\Delta\rho = 6$ (left) and (right) the spatio-temporal density evolution for manually driven cars ($\alpha = \beta = 0$ in (2))
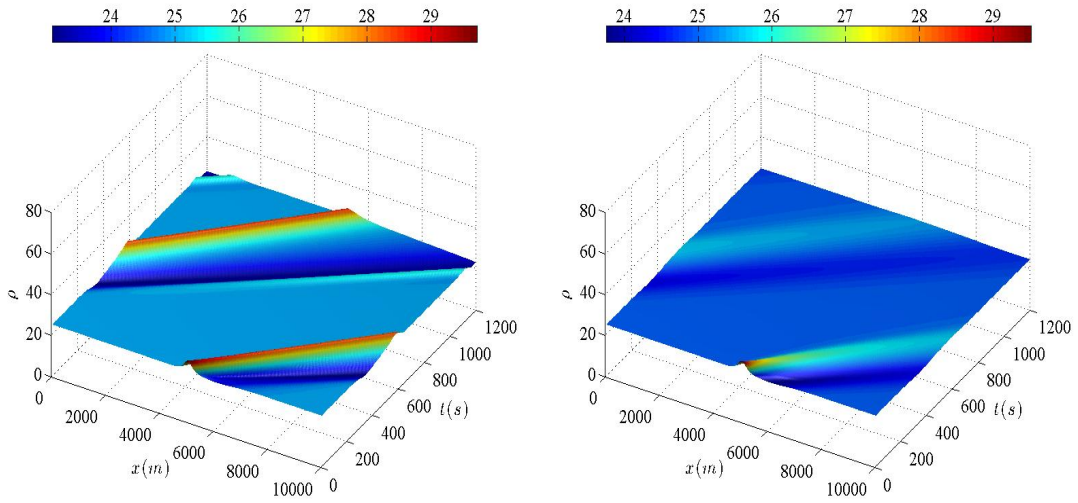

Figure 4: Density evolution for $\bar{\rho} = 25$ for ACC (left) and CACC traffic using (7)

19
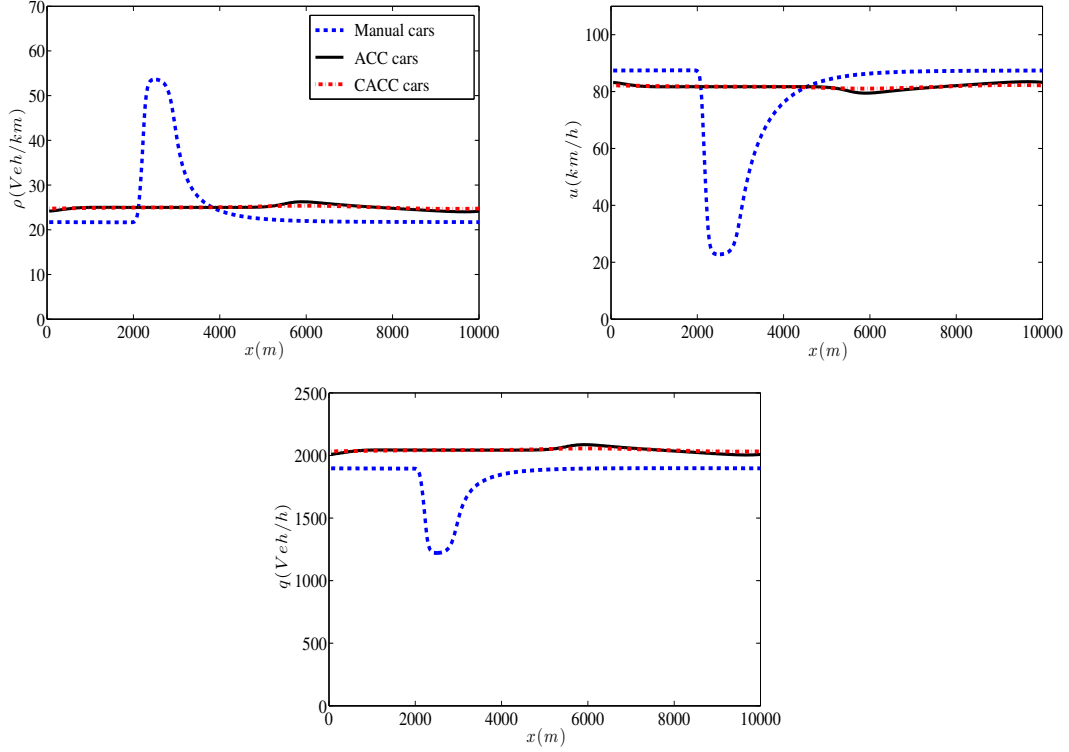
Figure 5: Density, velocity and flow profiles at $t = 1200s$ using (7) for $\bar{\rho} = 25$ and $\Delta\rho = 6$

In Figs 6 and 7 the results for the evolution of density for ACC and CACC traffic flows with the same initial conditions using the novel modeling equations (11) and (12) are presented. The coefficient $\tau^{\star} = 1s$ for ACC and the CACC coefficients $[\tau_1^{\star}, \tau_2^{\star}, \tau_3^{\star}] = [2, 3, 6]s$. The value for $\rho_{acc} = 0.9\rho_{cr}$ and two different values for $T^{\star}$ for CACC traffic are tested, $T^{\star} = 1.2$ and $T^{\star} = 1s$ while for ACC $T^{\star} = 1.2s$. We note here that these values for ACC and CACC systems correspond to a more conservative/considered driving behavior, compared to lower (although not very realistic with the current state-of-the-art) values, like $0.8s$ for ACC or even $0.5s$ for CACC, that correspond to more aggressive driving behavior. First, and comparing with the results of the previous ACC and CACC approach, a similar behavior is obtained. Both ACC and CACC flow are now stable with the initial perturbation traveling downstream. Only for the ACC flow the perturbation's amplitude slightly grows but then remains almost constant; while for the CACC traffic using $T^{\star} = 1s$ in (12) the perturbation dies out. This reduction of the $T^{\star}$ value from 1.2 to 1 for the CACC traffic has the expected effect of smoothing the traffic, as explained in Section 2, and can be affordable from CACC systems as a pre-specified parameter. This value of $T^{\star} = 1$ in (12) has been adopted in all the simulations that follow. In Fig. 7 the resulted uncongested, almost homogeneous, traffic can be

clearly seen along with an increased traffic flow rate along the total length of the ring road.

(a) ACC traffic for $T^{\star} = 1.2s$

(b) CACC traffic for $T^{\star} = 1.2s$

(c) CACC traffic for $T^{\star} = 1s$
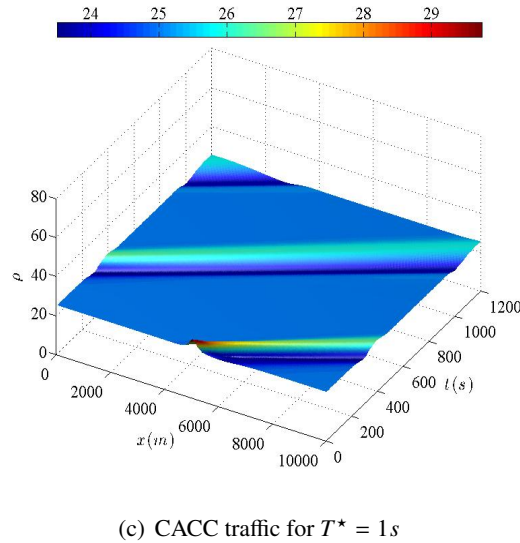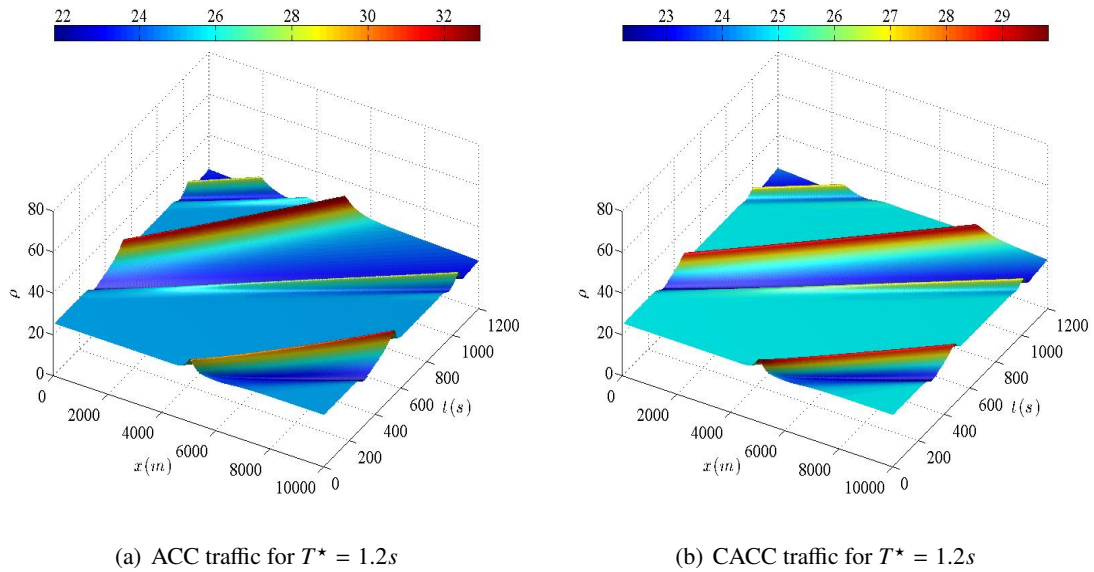
Figure 6: Density evolution for $\bar{\rho} = 25$ and $\Delta\rho = 6$ for ACC (left) and CACC traffic using (11) and (12)

Stop-and-go waves. The next scenario is for $\bar{\rho} = 35$ and $\Delta\rho = 6$ veh/km and all other parameters kept the same. Increasing $\bar{\rho}$ a cascade of traffic jams emerges, i.e. stop-and-go traffic, as can be seen
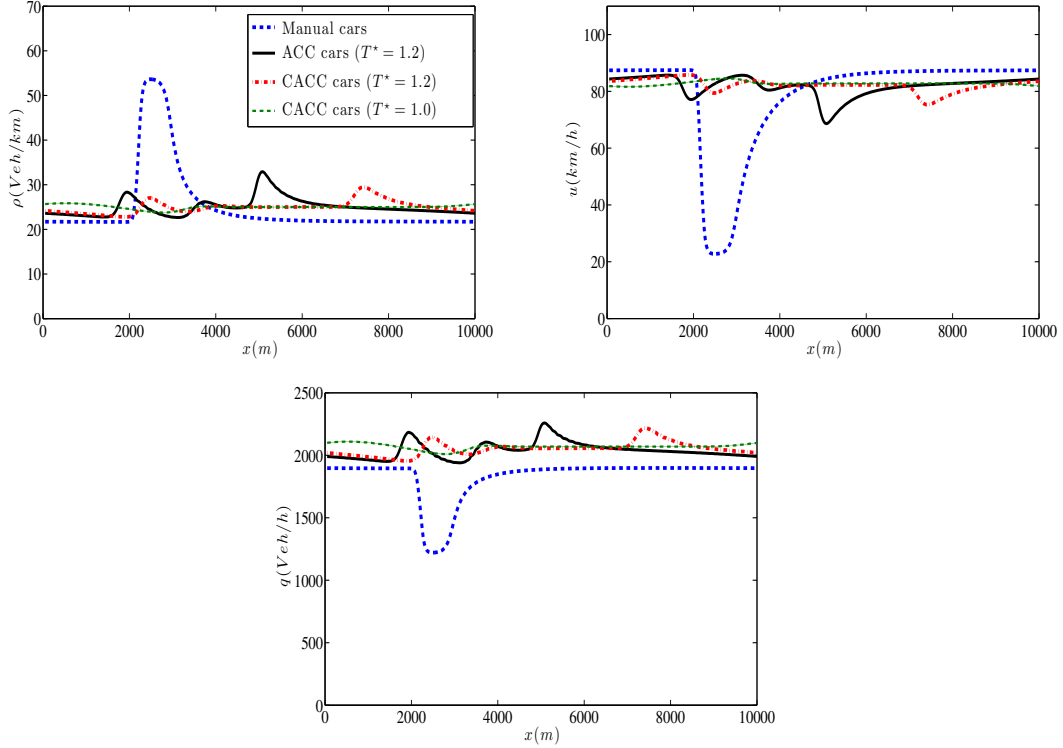
Figure 7: Density, velocity and flow profiles at $t = 1200s$ using (11) and (12) for $\bar{\rho} = 25$ and $\Delta\rho = 6$

in Fig. 8 for manually driven cars. In Fig. 9 the results for the evolution of density for ACC and CACC cars using (7) are shown. The initial homogeneous density belongs to the unstable regime for ACC vehicles, with the stop-and-go traffic becoming less profound; but to the stable regime for CACC traffic, with the perturbation traveling upstream and retaining an almost constant amplitude. In Fig. 10 the obtained profiles of density, speed and flow rate at $t = 1200s$ are shown for manual, ACC and CACC traffic. The resulted uncongested traffic behavior for CACC can be clearly seen in Fig. 10 along with an increased traffic flow rate in the total length of the ring road for ACC and CACC traffic. The simulation results presented here confirm the observation presented in [32] for a similar test case using the same set of parameters in (7).

Next, and in Fig. 11 the spatio-temporal evolution using the new ACC and CACC approach (11) and (12) are shown. The ACC traffic is still in the unstable regime, but remains uncongested; while for CACC traffic the initial perturbation rapidly fades out with time, leading to a homogeneous traffic. Referring to Fig. 12, it is important to note the increased traffic flow rate along the total length of the ring road for ACC and CACC traffic, which is more pronounced for CACC traffic, as a result of the imposed desired time gap at the proposed ACC and CACC approach.

22
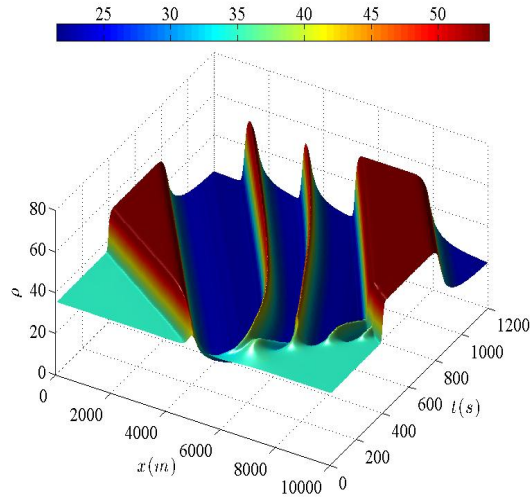
Figure 8: Spatio-temporal density evolution for manual cars for $\bar{\rho} = 35$ and $\Delta\rho = 6$
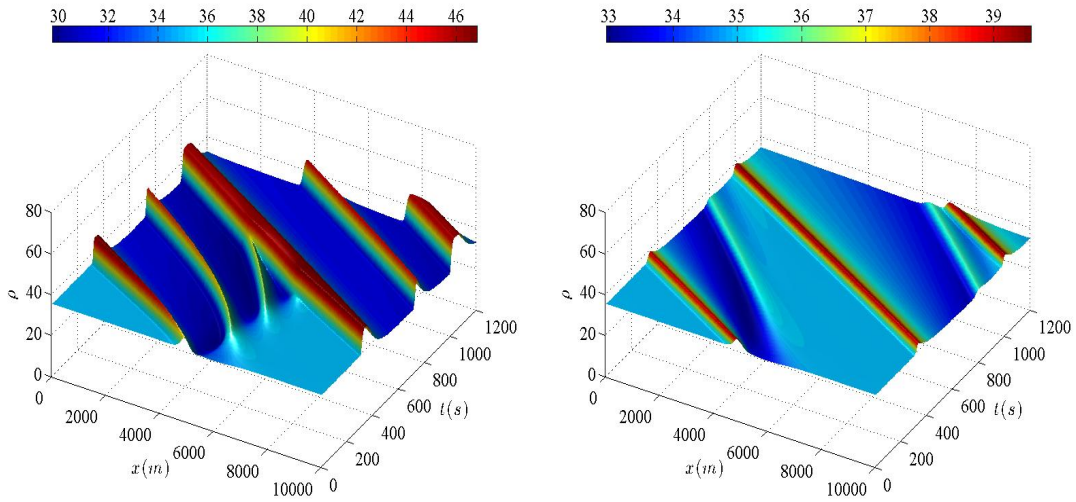
Figure 9: Density evolution for $\bar{\rho} = 35$ and $\Delta\rho = 6$ with ACC (left) and CACC traffic using (7)

Suppression of a traffic jump. The next scenario is for $\bar{\rho} = 28$ and $\Delta\rho = 60$ veh/km and all other parameters kept the same. Under these conditions the traffic flow is metastable, i.e., nonlinearly unstable with respect to perturbations exceeding a certain critical amplitude but otherwise stable

23
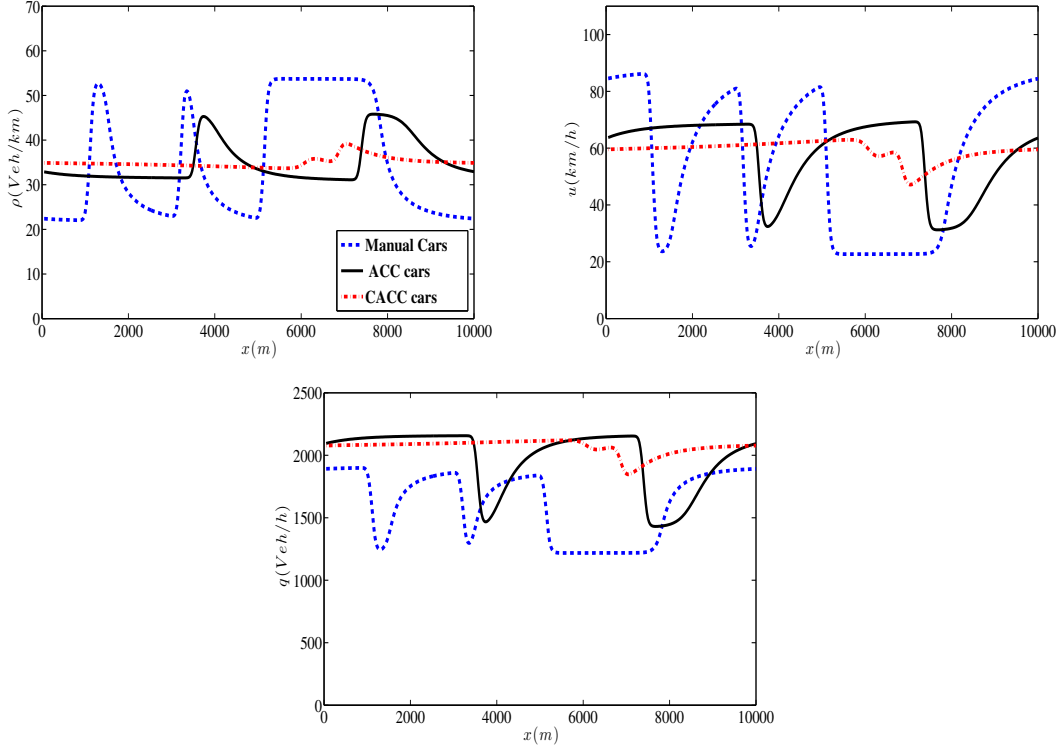
Figure 10: Density, velocity and flow profiles at $t = 1200s$ using (7) for $\bar{\rho} = 35$ and $\Delta\rho = 6$

[11]. As can be seen in Fig. 13, a persistent traffic jump is produced which propagates around the ring road. In Fig. 14 the results for the evolution of density for ACC and CACC cars using (7) are shown. For both ACC and CACC traffic the shock wave disappears since the positive peak of the large initial perturbation fades out quickly, in fact earlier in the CACC traffic. In Fig. 15 the spatio-temporal evolution using the new ACC and CACC approach (11) and (12) are presented. Similarly to the previous results, the smoothing of the initial perturbation can be observed, leading to uncongested and convectively stable traffic field. A noticeable difference in the CACC traffic here, compared to the previous approach, is the downstream propagation of the damped positive peak of the initial perturbation.

4.2. Traffic states close to an on-ramp

As it was analyzed in [47], the dynamics of ring roads or homogeneous infinite roads, i.e., closed systems, is controlled by traffic density. The dynamics of realistic roads, i.e., open systems with a bottleneck, is controlled by two flow-like quantities. The uncongested road sections are controlled by the inflow, and the congested sections by the (dynamic) bottleneck capacity.
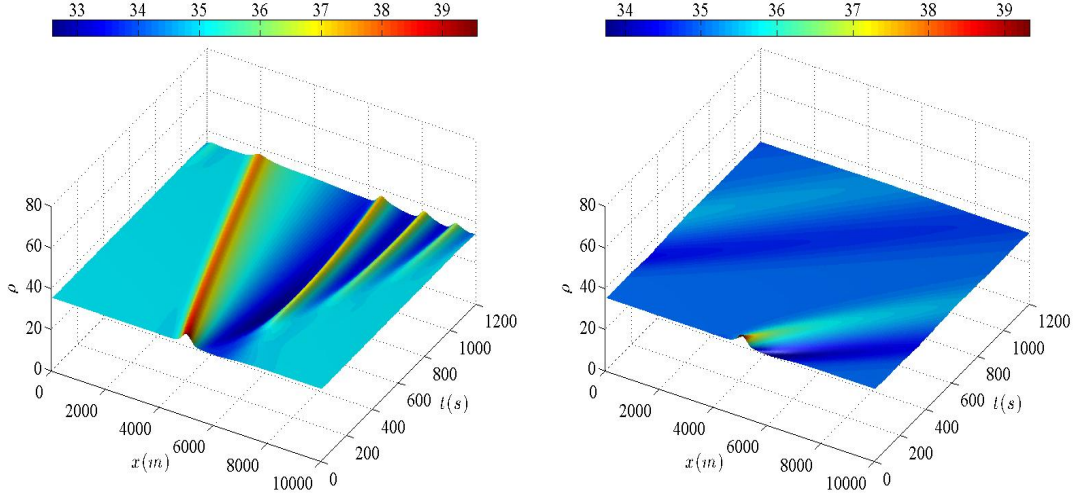
Figure 11: Density evolution for $\bar{\rho} = 35$ and $\Delta\rho = 6$ for ACC (left) and CACC flows using (11) and (12)

Different traffic states (i.e. congestion patterns) can be developed close to bottlenecks caused by on-ramps, lane closures, gradients etc. in a freeway. Here we investigate the different states that occur from an on-ramp flow. Varying the initial traffic density or flow, q_f, of the freeway, the ramp length, l_{rmp} and the ramp inflow, q_{rmp}, in the GKT model, leads to several interesting states of congested traffic. All these different congested states are observable in empirical traffic data, see [14, 16, 15, 17, 46, 47] and references therein. Our aim is to determine if the proposed ACC and CACC approaches can act as a sort of control measures to avoid the different resulting breakdowns of traffic; to this end, we must first verify the ability of the numerical model to reproduce such states as analyzed in [16, 15, 47]. Specifically, we simulate a single freeway lane, and two different sets of simulations were performed for an on-ramp of length $l_{rmp} = 400m$ at $x_{rmp} = 8000m$ with a merging zone for $x \in \left[x_{rmp} - l_{rmp}/2, x_{rmp} + l_{rmp}/2\right]$. The first set of simulations is for initial flow rates in the freeway on the "uncongested" side of the fundamental diagram, referring to Fig. 1, while the second for a flow rate on the "congested" side. The model parameters used in the simulations are, $u_{\max} = 110$ km/h, $\rho_{max} = 140$ veh/km, $\rho_{cr} = 0.27\rho_{max}$, $\tau = 40s$, $A_0 = 0.008$, $\delta A = 0.02$, $\delta\rho = 0.1\rho_{max}$, $T = 1.7s$ and $\gamma = 1.2$. In the numerical scheme, the number of grid points used was $npts = 400$ and the CFL value was set to 0.4.

For the first set of cases we simulate a freeway of length $L = 15$ km with open boundaries for a total of 120 minutes. To obtain stationary conditions, we simulate the first 20 minutes with a given homogeneous flow, q_f, on the freeway and a constant ramp inflow, q_{rmp}, applying homogeneous von Neuman boundary conditions at both ends of the freeway. Then we introduce a perturbation of amplitude δq_{rmp} by linearly increasing the ramp flow up to $q_{rmp} + \delta q_{rmp}$ at $t = 22.5min$, and
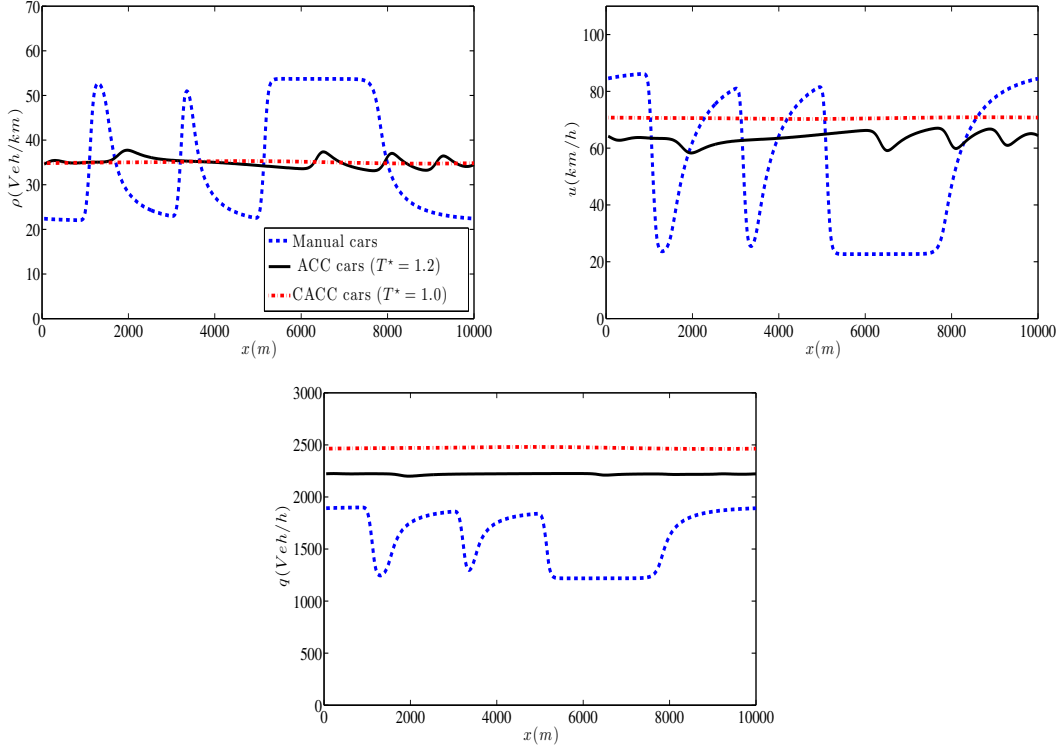
Figure 12: Density, velocity and flow profiles at $t = 1200s$ using (11) and (12) for $\bar{\rho} = 35$ and $\Delta\rho = 6$

decreasing it again to q_{rmp} by $t = 25min$. This perturbation on the ramp inflow corresponds to a temporary peak in the traffic inflow. When traffic breaks down at the bottleneck and congested traffic has formed upstream of it, one says that the bottleneck is activated. The different congested states that can be observed for manual traffic are presented next. It is noted that these states are observable in empirical traffic data as well [16, 15].

"Synchronized" homogeneous congested traffic (HCT). In this case, the initial homogeneous equilibrium traffic flow $q_f = 1350$ veh/h, without perturbations in the initial condition. The constant ramp inflow $q_{rmp} = 400$ veh/h and the on-ramp's perturbation amplitude $\delta q_{rmp} = 150$ veh/h. In the 120 minute simulation, shown in Fig. 16(a), the developed "synchronized" highly congested traffic can be observed. Here, a widening region of high density and low velocity is developed, but in there flow remains relatively high. This congested region's upstream front propagates upstream, while the downstream front is standing at the ramp.

Oscillating congested traffic (OCT). In this case, the initial homogeneous equilibrium traffic flow $q_f = 1540$ veh/h, the constant ramp inflow $q_{rmp} = 180$ veh/h and the on-rump's perturbation
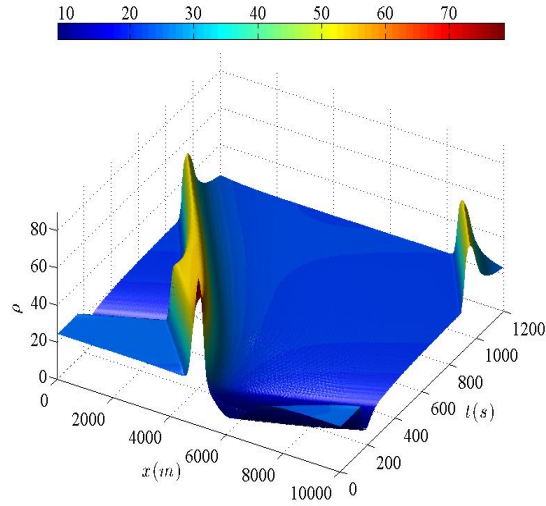
Figure 13: Spatio-temporal density evolution for manual cars for $\bar{\rho} = 28$ and $\Delta\rho = 60$
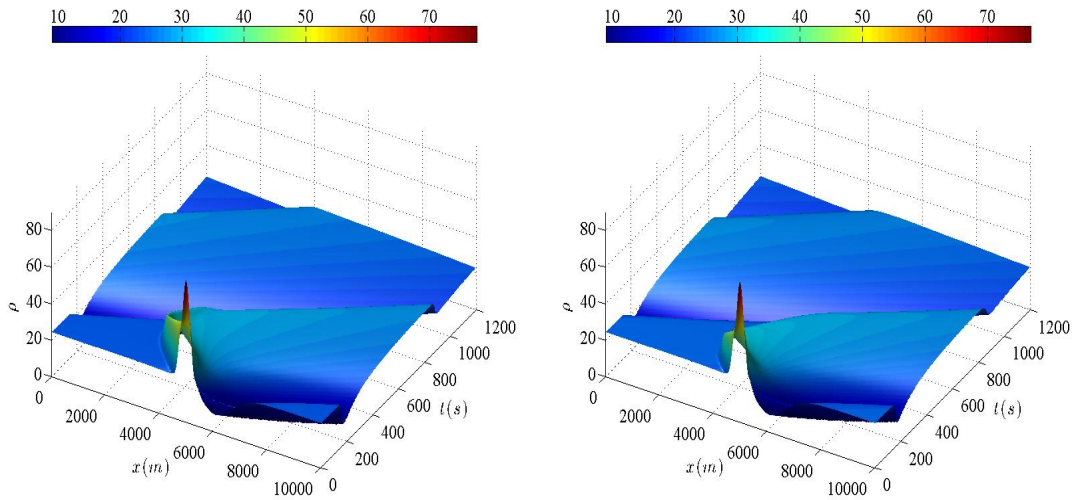
Figure 14: Density evolution for $\bar{\rho} = 28$ and $\Delta\rho = 60$ veh/km with ACC (left) and CACC flows using (7)

amplitude $\delta q_{rmp} = 180$ veh/h. The 120 minute of simulation spatio-temporal results for the traffic density are shown in Fig. 16(b) where a standing front at the ramp can be seen while the congested
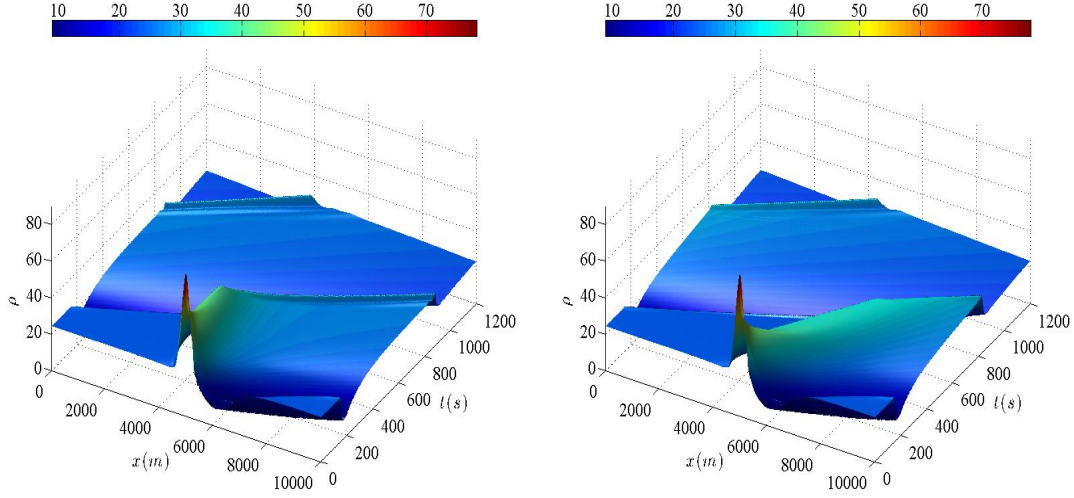
Figure 15: Density evolution for $\bar{\rho} = 28$ and $\Delta\rho = 60$ for ACC (left) and CACC flows using (11) and (12)

flow produced upstream oscillates.

Pinned localized cluster (PLC). In this case, the initial homogeneous equilibrium traffic flow $q_f = 1425$ veh/h, the constant ramp inflow $q_{rmp} = 200$ veh/h and the on-rump's perturbation amplitude $\delta q_{rmp} = 400$ veh/h. The spatio-temporal results for the traffic density are shown in Fig. 16(c) where the pinned at the rump localized congestion can be observed.

Triggered stop-and-go waves (TSG). In the final case, the initial homogeneous equilibrium traffic flow $q_f = 1690$ veh/h, the constant ramp inflow $q_{rmp} = 75$ veh/h and the on-rump's perturbation amplitude $\delta q_{rmp} = 75$ veh/h. The simulation spatio-temporal results for the traffic density are shown in Fig. 16(d) where the traffic stop-and-go waves evolution can be seen.

All the results are consistent with those in [16, 15] for the same set of parameters in the GKT model and in all cases the induced perturbation in δq_{rmp} causes the breakdown in traffic close to the on-ramp. The perturbation travels downstream as long as it is small and upstream as it becomes larger and eventually activates the bottleneck associated with the on-ramp. Applying ACC or CACC to these situations alleviates the problem of traffic breakdown. As can be seen in Fig. 17, applying approach (7) and then (11) and (12) produces very similar results in all cases (here, and for brevity, we only present the one that corespondents to PLC traffic for manual cars). Activation of ACC and CACC dynamically increases the local capacity near the on-ramp, thus free flow occurs both upstream and downstream of the on-ramp.

Having verified that the numerical model can reproduce the different traffic breakdown states, for initial flow rates in the freeway on the "uncongested" side of the fundamental diagram, we

(a) HCT

(b) OCT

(c) PLC

(d) TSG
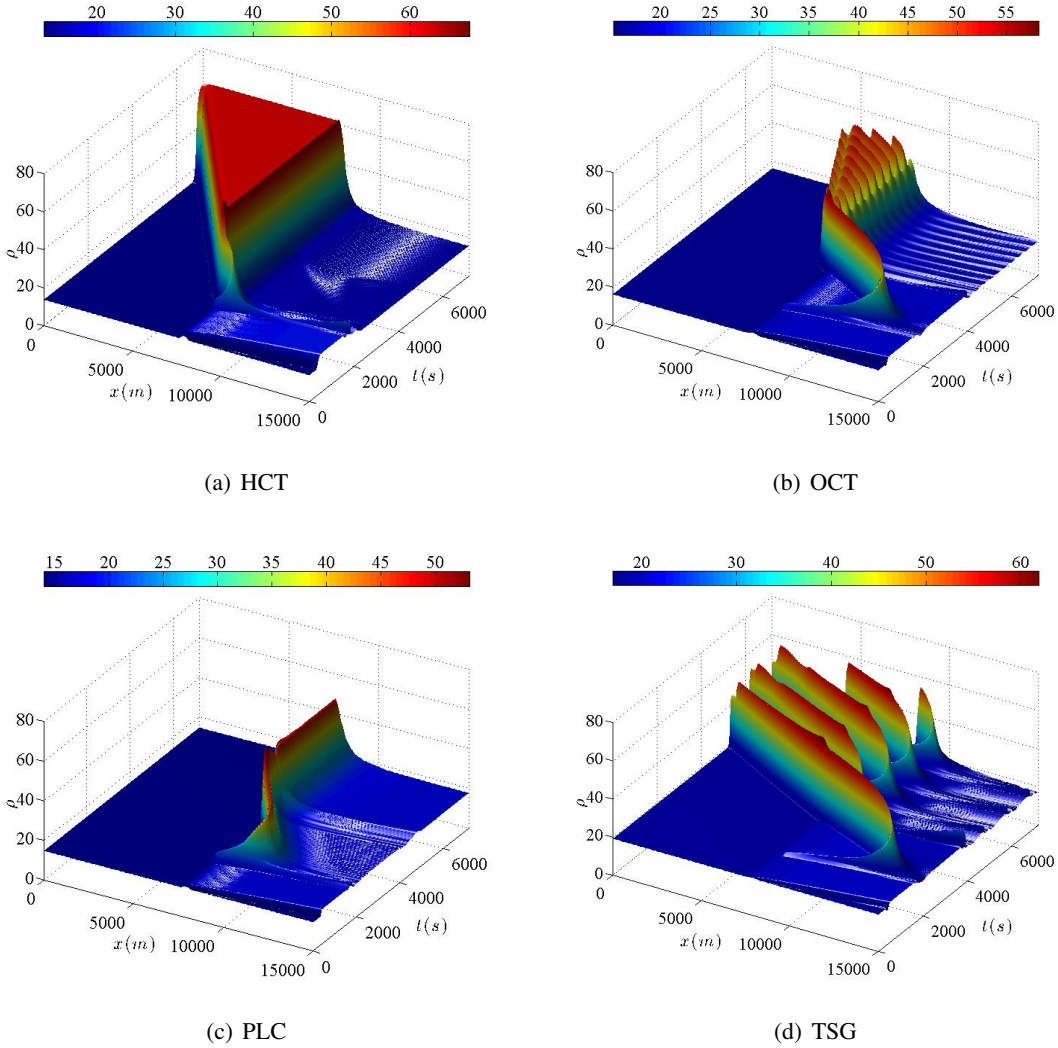
Figure 16: Density evolution of different traffic states close to an on-ramp for manual cars

next present the second set of test cases for an initial flow rate on the "congested" side. For these cases, we simulate a freeway of length $L = 30km$ with open boundaries for a total of 150 minutes. Keeping the initial homogeneous equilibrium traffic flow $q_f = 1824.5$ veh/h (which results to $\rho_{initial} = \rho(x, 0) = 30$ veh/km) we vary only the ramp inflow q_{rmp} to obtain different scenarios. No perturbation to q_{rmp} is imposed, i.e. $\delta q_{rmp} = 0$, and all other model and computational parameters remain the same. It is important to note that, following from the phase diagram of the traffic states forming in the vicinity of an on-ramp in [14, 16, 15], similar situations are expected to emerge as
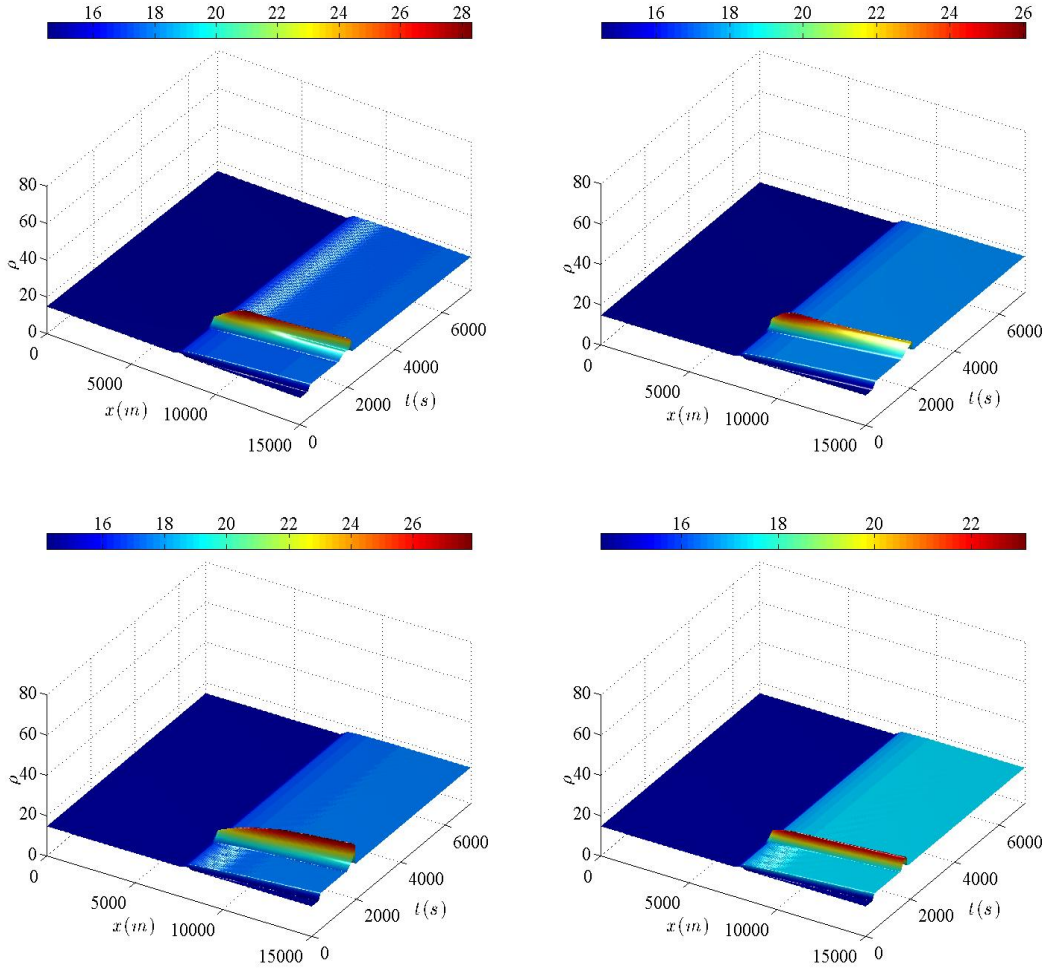
Figure 17: Density evolution for traffic states close to an on-ramp for ACC and CACC traffic using (7) (top) and using (11) and (12) (bottom)

in the previous set of cases. Keeping q_f constant in each case but decreasing the ramp inflow q_{rmp} different traffic flow regimes can be observed. Our aim here is to quantify the effects of the different ACC and CACC approaches on the resulted traffic flow fields.

The first case here is for $q_{rmp} = 400$ veh/h. The traffic density evolution for manual traffic is presented in Fig. 18. One can observe the HCT upstream of the ramp and the moving localized clusters produced downstream of the ramp. These clusters need almost two hours before disappearing from the flow field.

In Fig. 19 the spatio-temporal evolution for ACC and CACC traffic using (7) is presented and
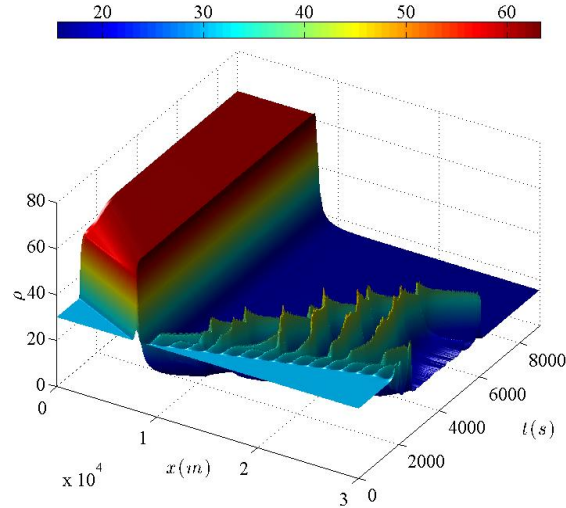
Figure 18: Density evolution close to an on-ramp for manual cars for $q_{rmp} = 400$ veh/h

in Fig. 20 the density, velocity and flow rate profiles at $t = 150min$ are compared between each other and those resulted from manual traffic. As it can be observed, the ACC traffic produces an oscillatory, but uncongested, flow downstream of the ramp but reduces the HCT upstream. The CACC application stabilizes the downstream flow but retains the average values of the traffic flow.

In Fig. 21 the spatio-temporal evolution for ACC and CACC traffic using (11) and (12) is presented, and in Fig. 22 the density, velocity and flow rate profiles at $t = 150min$ are compared between each other and those resulted from manual traffic. Activation of ACC stabilizes the traffic downstream of the ramp and at the same time greatly increases the flow both upstream and downstream, while the upstream HCT congestion is reduced. For CACC the HCT region is propagating at a much lower speed upstream, while an increased homogeneous flow is produced downstream of the on-ramp. Moreover, the resulted flow upstream is almost uniform despite the formation of HCT. The increased flow rate for the CACC traffic compared to the ACC one is mainly attributed to the reduced value of the imposed time-gap, $T^{\star}$, in (12) which leads to an increased bottleneck capacity.

The second case is for $q_{rmp} = 200$ veh/h. The traffic density evolution for manual traffic is presented in Fig. 23. One can observe the OCT flow upstream of the ramp and stop-and-go waves downstream. These stop-and-go waves initially travel downstream but at later times start traveling upstream converging to the oscillatory congested region upstream of the ramp. Whenever an upstream traveling jam passes the bottleneck, it triggers a new perturbation

In Fig. 24 the spatio-temporal evolution for ACC and CACC traffic using (7) is presented. Both the ACC and CACC traffic have become stable upstream of the ramp, but the ACC traffic remains

31
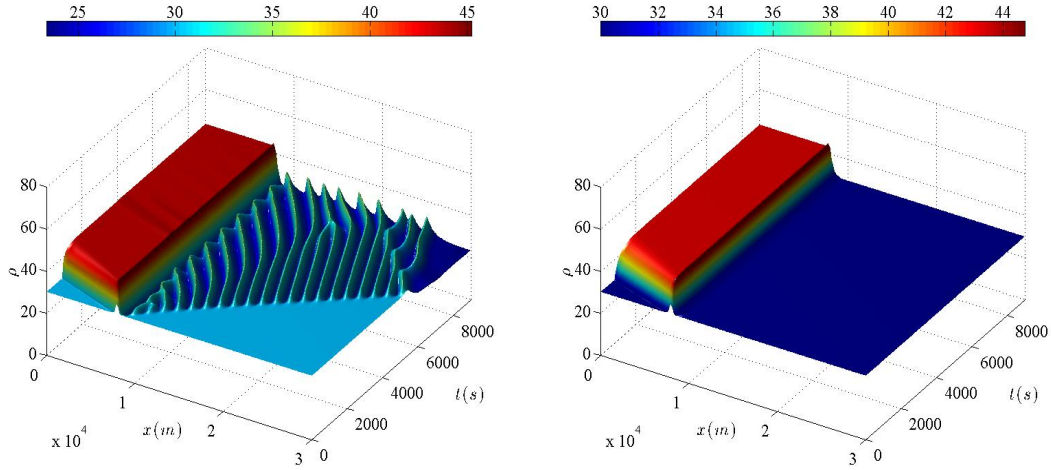
Figure 19: Density evolution with q_{rmp} = 400 veh/h for ACC (left) and CACC traffic using (7)

oscillatory downstream. Similar to the previous case, both ACC and CACC flows retain the same average values as can be seen in Fig. 25

In Fig. 26 the spatio-temporal evolution for ACC and CACC traffic using (11) and (12) is presented and in Fig. 27 the density and flow rate profiles at $t = 150min$ are compared between each other and those resulted from manual traffic. The ACC traffic becomes non-oscillatory both upstream and downstream of the ramp but an HCT region slowly develops upstream, but the downstream flow rate is greatly increased. For the CACC traffic the upstream congestion has completely disappeared and a more pronounced increase in the flow rate is established.

The last case is for q_{rmp} = 75 veh/h. The traffic density evolution for manual traffic is presented in Fig. 28. One can observe the TSG flow upstream of the ramp and the formation of stop-and-go waves downstream of the ramp. These downstream stop-and-go waves initially travel with the flow but at later times start traveling against the flow, converging to the TSG region upstream of the ramp.

In Fig. 29 the spatio-temporal evolution for ACC and CACC traffic using (7) is shown, while the density and flow rate profiles at $t = 150min$ are compared between each other and those resulted from manual traffic in Fig. 30. The ACC traffic remains oscillatory both downstream and upstream of the ramp. Actually the downstream oscillations enter the higher density region upstream of the ramp and generate additional ones. For the CACC the traffic is now non-oscillatory but the density downstream of the ramp is not affected by the incoming ramp flow and remains unchanged.

Fig. 31 presents the spatio-temporal evolution for ACC and CACC traffic using (11) and (12). For both ACC and CACC traffic the resulting flows are now uncongested and stable with increased flow rates. As it can be seen in Fig. 32 the vehicles' increased average velocity has become uniform
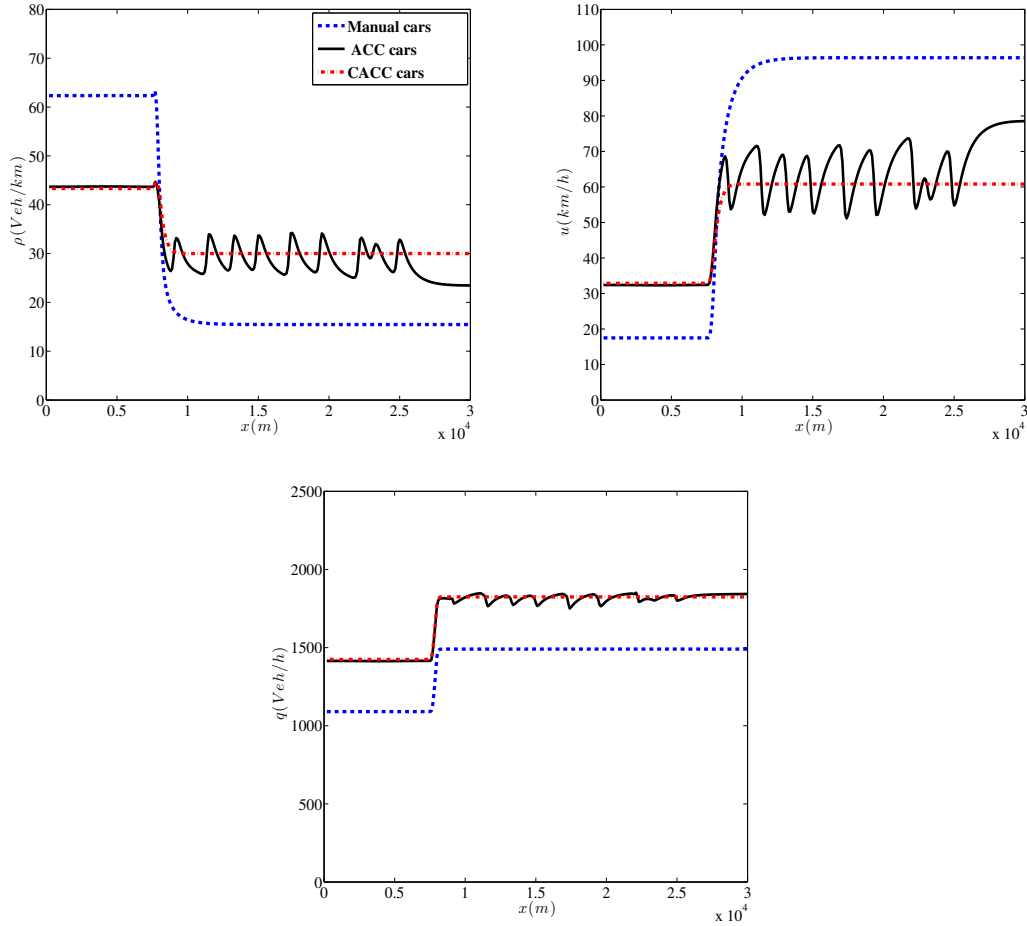
Figure 20: Density, velocity and flow rate profiles at $t = 150min$ for $q_{rmp} = 400$ veh/h using (7) for ACC and CACC

throughout the entire domain for CACC traffic.

5. Conclusions

This work presents two macroscopic approaches to model the dynamics of ACC and CACC traffic flows. To model the impact of ACC and CACC vehicles on traffic flow dynamics, as described by the two approaches, the second-order GKT model was used as the basis model since it allows to describe the fluctuations of speed dynamics around a so-called equilibrium speed-density relationship. An important part of the simulation process is the numerical solution of the resulting models by the development of a high-resolution finite volume relaxation scheme. The first approach to ACC and CACC was adapted from Ngoduy [32] where the core idea was to represent the
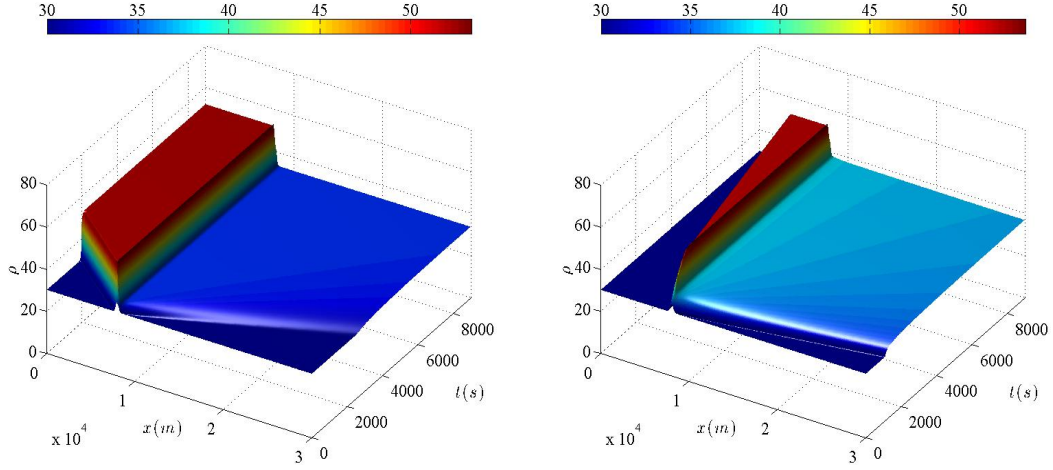
Figure 21: Density evolution with $q_{rmp} = 400$ veh/h for ACC (left) and CACC traffic using (11) and (12)

instantaneous response of the ACC and CACC due to changes of the speed of the leader(s) by the introduction of a relaxation acceleration/deceleration term in the momentum equation of the GKT model. The second approach presented here is a novel one and is based on the introduction of a new relaxation term in the momentum equation that satisfies the time/space-gap principle of ACC systems. Further, in the new approach the original GKT non-local interaction term is smoothly switched off by the Fermi-like function and replaced by the new relaxation term such that in congested traffic flow this term takes over. In both approaches, the relaxation time is distributed over multiple vehicles in the CACC systems whereas in the ACC ones the relaxation time is only related to the direct leading vehicle. Thus, the effects of ACC vehicles have been extended to account for the information exchange between multiple vehicles. Although the two approaches introduce a relaxation source term in the second equation of the GKT model, there is an important fundamental difference between them in terms of which ACC criteria are satisfied. It should be noticed that by setting shorter time-gap and short relaxation time, for example, $T = 1s$ and $\tau = 5s$, in the original GKT model will produce similar dynamics as that of the (C)ACC approaches presented. However, in our approach, the constant time gap $T^\star$ is imposed through its corresponding effect on the desired density $\rho^\star$, via eq. (10) for ACC, and the flow eventually is forced to relax to this (desired) $\rho^\star$.

To study the performance and effects of the two approaches, as well as their differences, in the traffic flow characteristics, two main categories of test cases were presented in the numerical simulations. The first one is for flows on a circular homogeneous freeway (with periodic boundary conditions) with respect to small and large perturbations introduced. The second is the simulation of a freeway with an on-ramp (i.e. a potential bottleneck) where open boundary conditions have
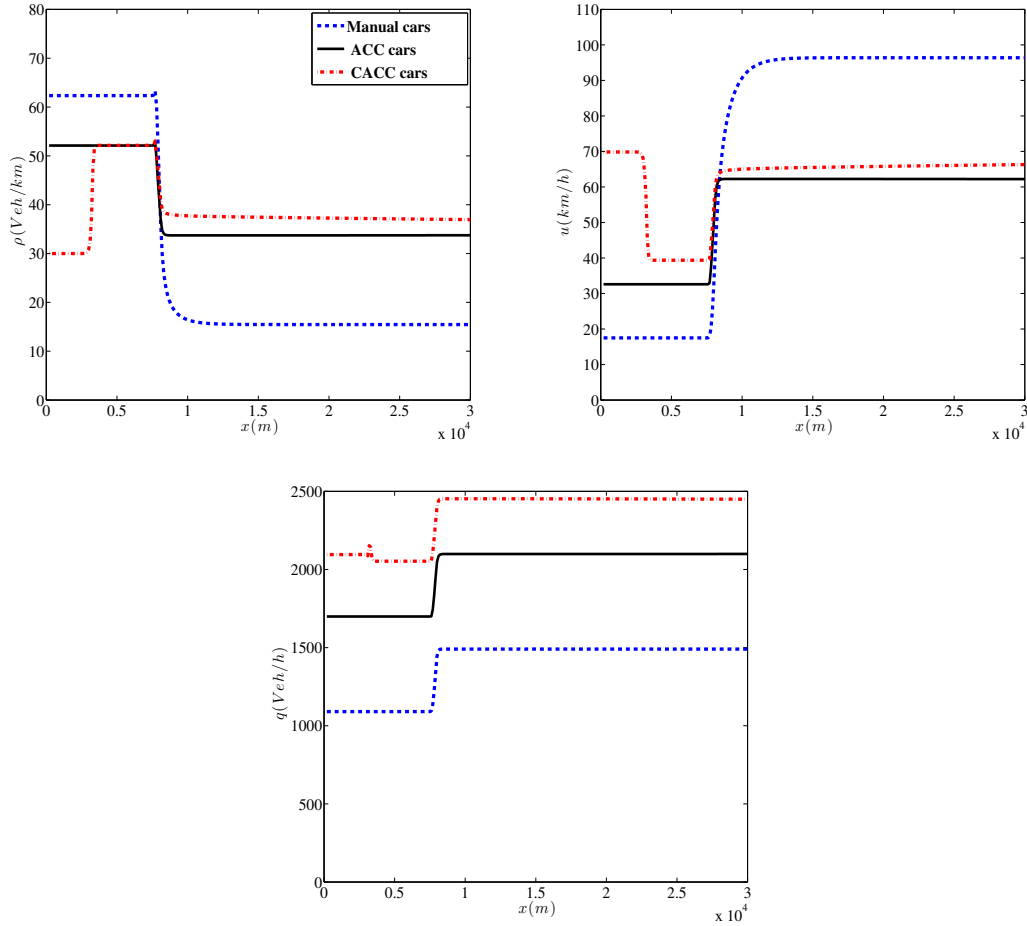
Figure 22: Density, velocity and flow rate profiles at $t = 150min$ for $q_{rmp} = 400$ veh/h using (11) and (12)

been used. In all the tests performed in the first category, the formation of traffic instabilities with respect to initial perturbations for different car types (CACC, ACC and manual vehicles) has been investigated. We have shown numerically that for both approaches CACC vehicles enhance the stabilization of traffic flow with respect to both small and large perturbations compared to ACC vehicles. Each approach has its own effects to the dynamics of traffic flow, but generally leads to the stabilization of the flow due to disturbances. This is in accordance with the analytical and numerical findings presented in [32]. However, and although both modelling approaches lead to comparable qualitative results, in some cases different shock-wave propagation patterns can also be observed due to the different contribution of the ACC/CACC term for each model.

A major deference between our approach and that in [32] is the observed enhanced dynamic
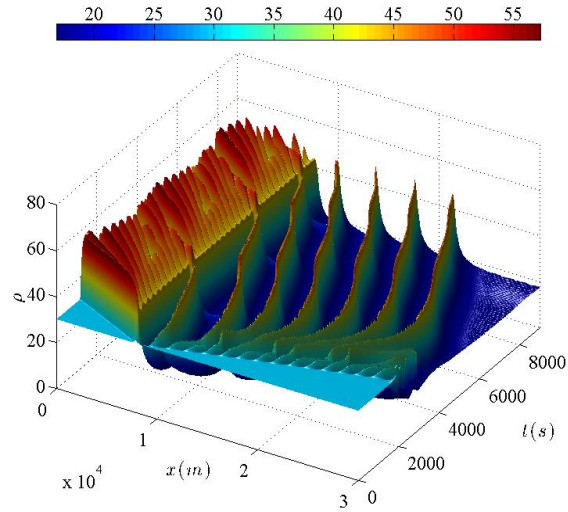
Figure 23: Density evolution close to an on-ramp for manual cars for q_{rmp} = 200 veh/h
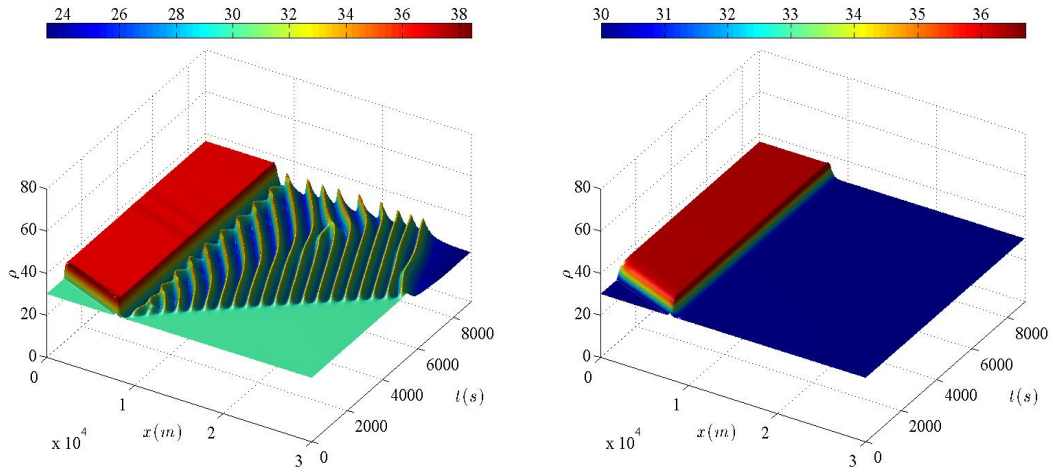

Figure 24: Density evolution with q_{rmp} = 200 veh/h for ACC (left) and CACC traffic using (7)

equilibrium capacity for our CACC system due to the satisfaction of the time/space-gap principle. For the second category of test cases, both approaches lead to more anticipative driving behavior in the congested traffic situations, which leads to the suppression of the oscillation waves, so that
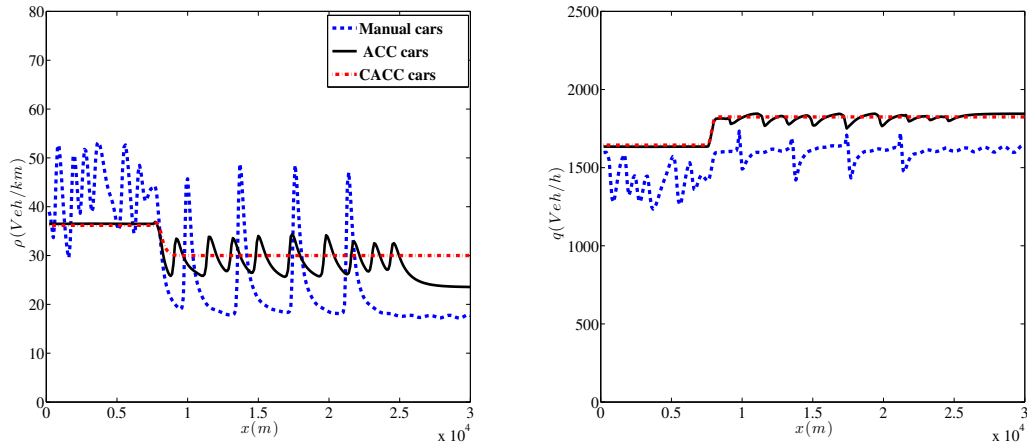
Figure 25: Density and flow rate profiles at $t = 150min$ for $q_{rmp} = 200$ veh/h using (7) for ACC and CACC
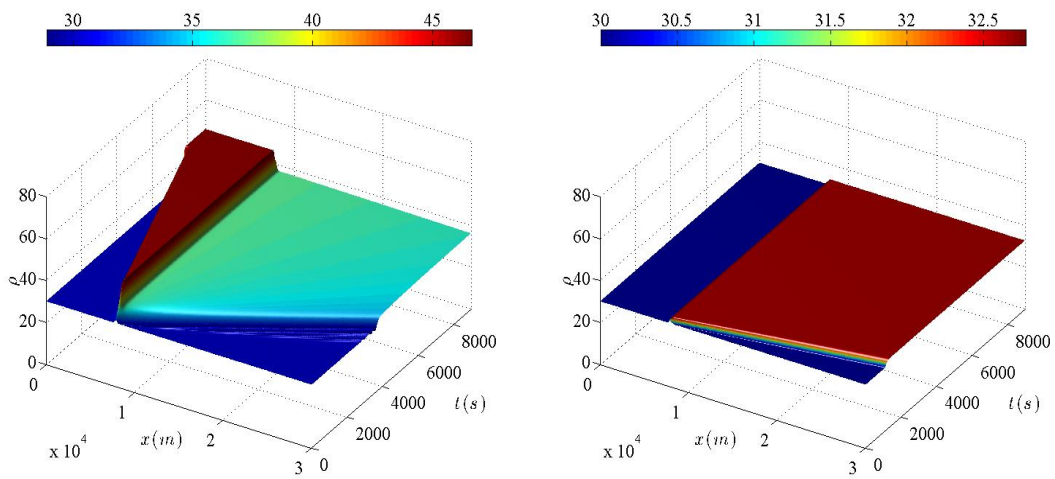
Figure 26: Density evolution with $q_{rmp} = 200$ veh/h for ACC (left) and CACC traffic using (11) and (12)

the traffic is convectively stable near the on-ramp. From the numerical results, we can conclude that, by applying ACC and CACC systems, the flow becomes stabilized with respect to on-ramp perturbations (temporary inflow peaks) and all oscillation waves caused near a bottleneck can be eliminated for densities on the ungongested side of the fundamental diagram. The observed enhanced dynamic equilibrium capacity for our CACC system resulted to the suppression of traffic congestion at the on-ramp bottleneck, improved outflow from the bottleneck and harmonization of
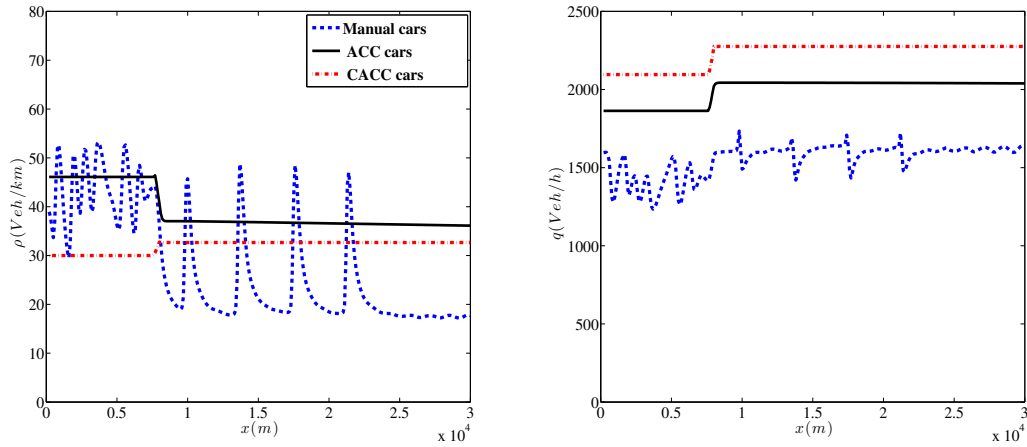
Figure 27: Density and flow rate profiles at $t = 150min$ for $q_{rmp} = 200$ veh/h using (11) and (12)
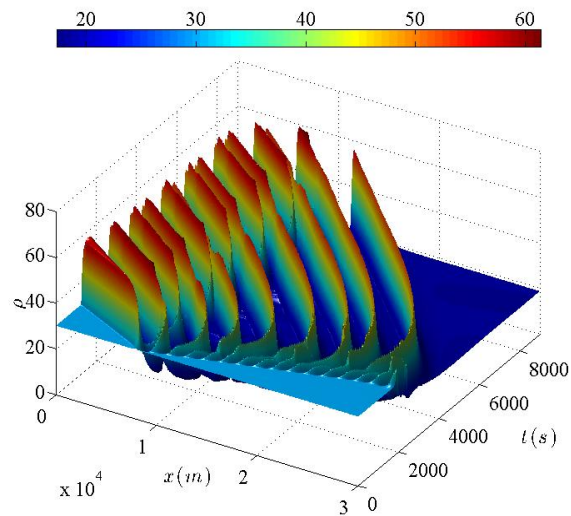

Figure 28: Density evolution close to an on-ramp for manual cars for $q_{rmp} = 75$ veh/h

the average speed for higher inflow values from the ramp and main flow in the congested side of the fundamental diagram, compared to Ngoduy's approach. As a bottleneck is defined by a capacity reduction, the inclusion of the time/space-gap principle in our CACC approach manages to fill the capacity gap at the bottleneck. We postulate that, this approach of jam-avoiding driving by CACC

38
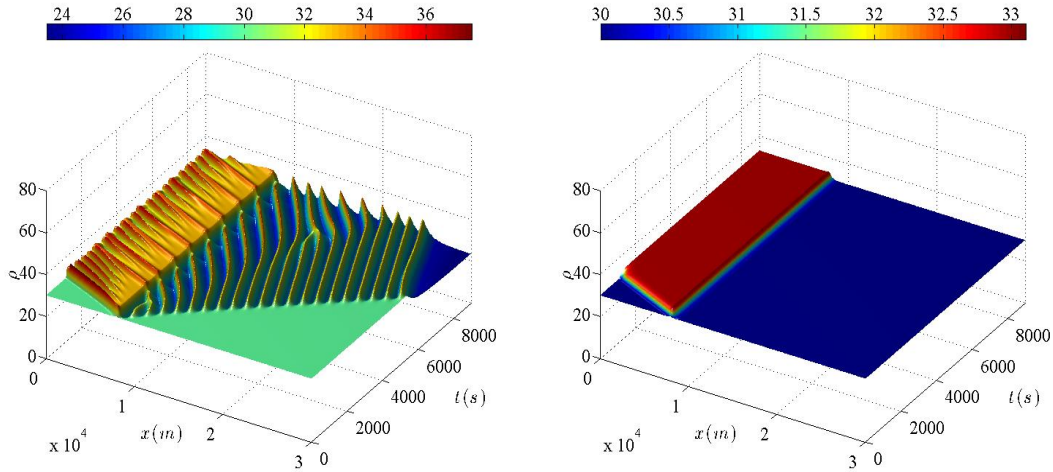
Figure 29: Density evolution with $q_{rmp} = 75$ veh/h for ACC (left) and CACC traffic using (7)
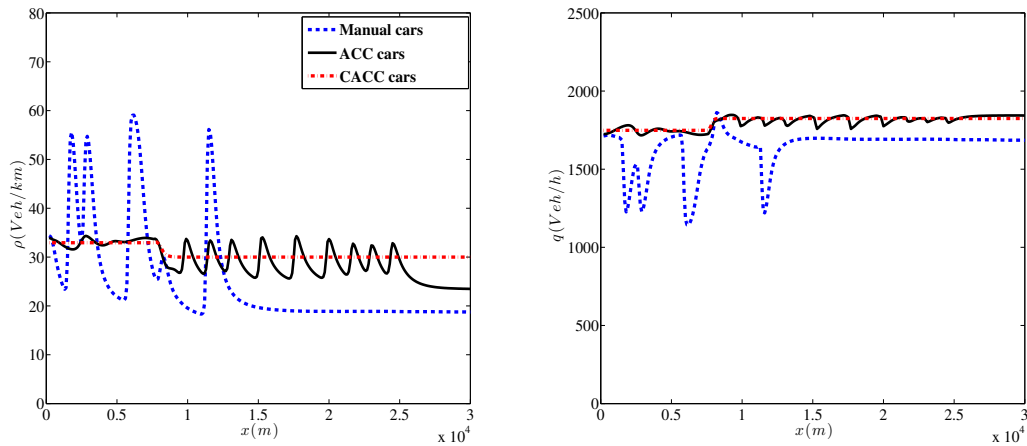

Figure 30: Density and flow rate profiles at $t = 150min$ for $q_{rmp} = 200$ veh/h using (7) for ACC and CACC

vehicles, which dynamically increases the local capacity near the on-ramp, can be transferred to other kinds of bottlenecks as well thus enhancing traffic operations.

Following from this work, we can argue that the proposed ACC and CACC approach, along with its accurate numerical approximation, can provide a macroscopic insight into the dynamics of intelligent traffic flow. Our ongoing work is the numerical investigation of the characteristics of mixed traffic flow consisting of CACC and manual vehicles to access the contribution of the
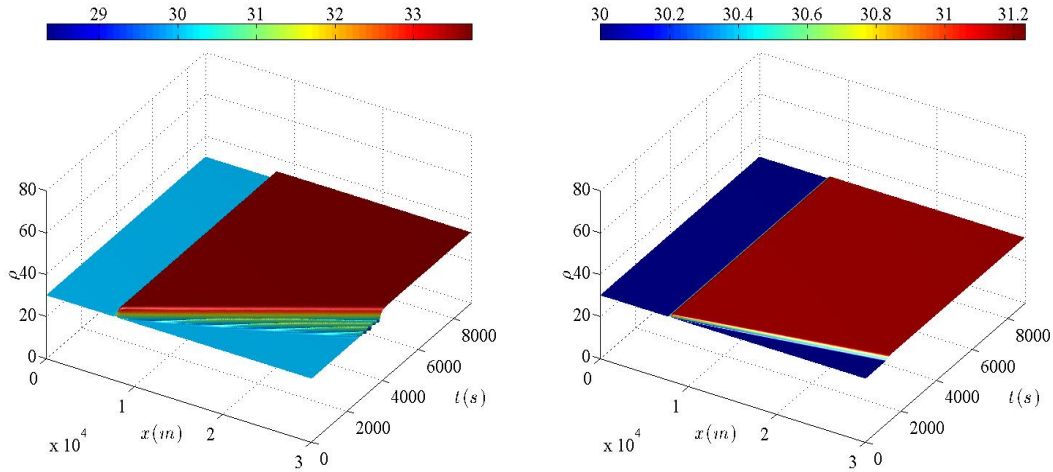
Figure 31: Density evolution with q_{rmp} = 75 veh/h for ACC (left) and CACC traffic using (11) and (12)

penetration rate of CACC vehicles to the stabilization of the traffic dynamics. In addition, further validation of the proposed ACC/CACC approach compared to microscopic simulations is under development.

Acknowledgments

References

[1] Alkim T.P., Schuurman H. and Tampere C.M.J., Effects of External Cruise Control and Co-operative Following on Highways: an analysis with the MIXIC Traffic Simulation Model. Proceedings of the IEEE Intelligent Vehicles Symposium of the Institute of Electrical and Electronics Engineers, 474-479, 2000.

[2] Arnaout G.M. and Bowling S., A Progressive deployment strategy for Cooperative Adaptive Cruise Control to improve traffic dynamics, *International Journal of Automation and Computing*, **11**: 10-18, 2014.

[3] Ascher U., Ruuth S. and Spiteri R., Implicit-explicit Runge-Kutta methods for time-dependent partial differential equations, *Appl. Numer. Math.*, **25**:151-167, 1997.
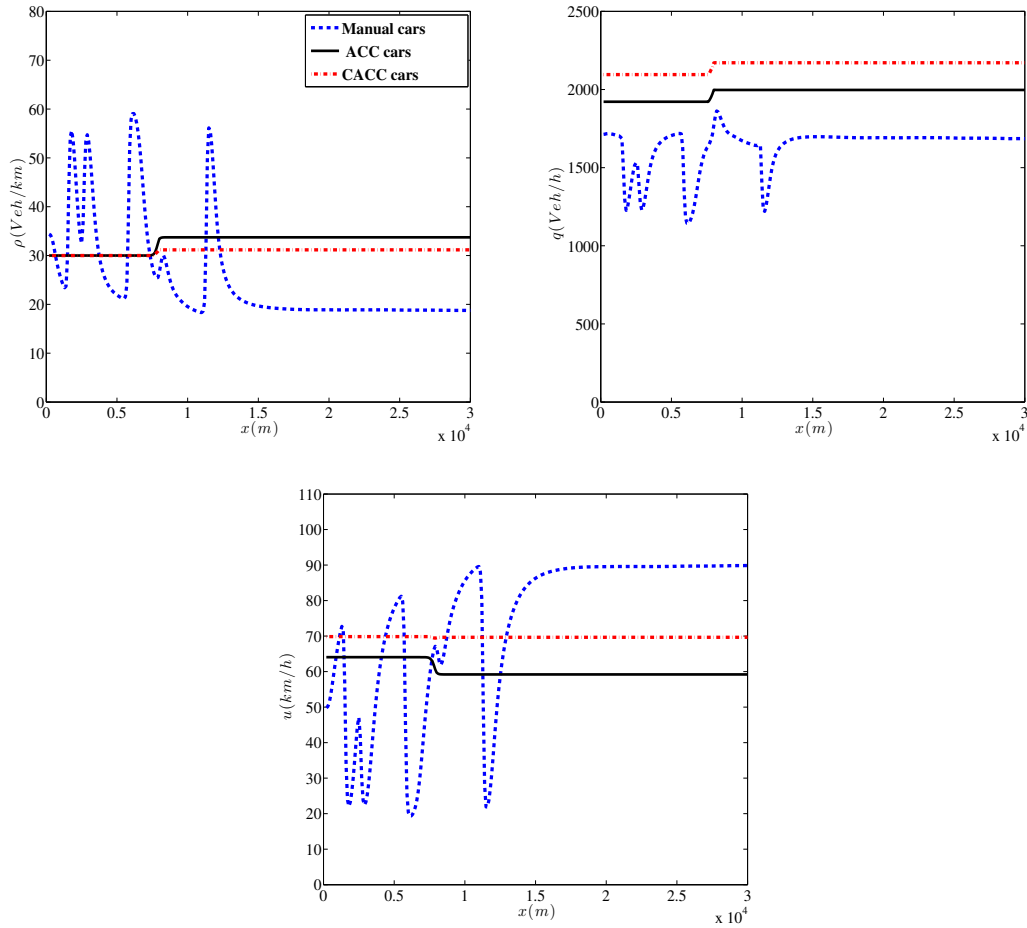
Figure 32: Density, flow rate and velocity profiles at $t = 150min$ for $q_{rmp} = 75$ veh/h using (11) and (12)

[4] Borsche R., Kimathi M., Klar A., A class of multi-phase traffic theories for microscopic, kinetic and continuum traffic models, *Comput. Math. Appl.*, **64**:2939-2953, 2012.

[5] Borges R., Carmona M., Costa B. and Don W.-S., An improved weighted essentially non-oscillatory scheme for hyperbolic conservation laws, *J. of Comp. Phys.*, **227**:3191-3211, 2008.

[6] Chalabi A. and Seghir D., Convergence of relaxation schemes for initial boundary value problems for conservation laws, *Comput. Math. Appl.*, **43** (8-9):1079-1093, 2002.

[7] Delis A.I., Nikolos I.K and Papageorgiou M. High-resolution numerical relaxation approximations to second-order macroscopic traffic flow models, *Transportation Research Part C: Emerging Technologies*, **44:**318-349, 2014.

[8] Davis L.C., Effect of adaptive cruise control systems on traffic flow, *Physical Review E*, **69**:066110-7, 2004.

[9] Davis, L.C., 2007. Effect of adaptive cruise control systems on mixed traffic flow near an on-ramp. *Physica A*, **379**:274-290, 2007.

[10] Demir C., Modelling the impact of ACC-Systems on the Traffic Flow at Macroscopic Modeling Level. Traffic and Granular Flow '01, pp. 305-317, 2003.

[11] Helbing D. and Treiber M., Numerical simulation of macroscopic traffic equations, *Computing in Science and Engineering*, **1**(5):89-99, 1999.

[12] Helbing D., Traffic and related self-driven many-particle systems, Reviews of Modern Physics, **73**:1067-1141, 2001.

[13] Helbing D. and Treiber, M., Gas-kinetic-based traffic model explaining observed hysteretic phase transition, *Physical Review Letters*, **81**(14):3042-3048, 1998.

[14] Helbing D., Hennecke A. and Treiber M., Phase diagram of traffic states in the presence of inhomogeneities, *Physical Review Letters*, **82**(21):4360-4363, 1999.

[15] Helbing D., Hennecke A., Shvetsov V. and Treiber M., MASTER: Macroscopic traffic simulation based on a gas-kinetic, non-local traffic model, *Transportation Research Part B: Methodological*, **35**(2):183-211, 2001.

[16] Helbing D., Hennecke A., Shvetsov V. and Treiber M., Micro- and macro-simulation of freeway traffic, Mathematical and Computer Modelling, **35**:517-547, 2002.

[17] Helbing D., Treiber M., Hennecke A. and Schönhof, Theoretical vs empirical classification and prediction of congested traffic states, *The European Physical Journal B*, **69**:583-598, 2009.

[18] Hermann M. and Kerner B.S., Local cluster effects in different traffic flow models *Physica A*, **255**:163-198, 1998.

[19] Herty M., Pareschi, L. and Seaid M., Discrete-velocity models and relaxation schemes for traffic flows, *SIAM J. Sci. Comput*, **28**:1582-1596, 2006

[20] Hoogendoorn S.P. and Bovy, P.H.L. Model assessment of dynamic speed limit control. In WCTRS, World conference on transport research (pp. 1-20). Seoul, Korea: WCT-research society, 2001

[21] Hoogendoorn S.P., Minderhoud M.M., 2001. ADAS impact assessment by micro-simulation, *European Journal of Transport and Infrastructure Research*, **1**:255-275, 2001.

[22] Kesting A., Treiber M., Schönhof M. and Helbing D., Adaptive Cruise Control Design for Active Congestion Avoidance, *Transportation Research Part C*, **16**:668-683, 2008.

[23] Kesting A., Treiber M. and Helbing D., Enhanced Intelligent Driver Model to Access the Impact of Driving Strategies on Traffic Capacity, *Philosophical Transactions of the Royal Society A*, **368**:4584-4605, 2010.

[24] Jin S. and Xin Z., The relaxing schemes of conservation laws in arbitrary space dimensions, *Comm. Pure Appl. Math.*, **48**:235–277, 1995.

[25] Lenz H., 1999. Entwicklung nichtlinearer, diskreter Regler zum Abbau von Verkehrsflussinhomogenitaeten mithilfe makroskopischer Verhkehrsmodelle, Ph.D dissertation, Lehrstuehl fuer Mensch-Maschine-Kommunikation, Fakultaet fuer Elektrotechnik und Informationstechnik der Technischen Universitaet Muenchen, Shaker Verlag, Aachen.

[26] Liu T.P., Hyperbolic conservation laws with relaxation, *Comm. Math. Phys.*, **108**:153-175, 1987.

[27] Marsden G., McDonald M.and Braxkstone M., Towards an understanding of adaptive cruise control, *Transportation Research Part C: Emerging Technologies*, **9**:3351, 2001.

[28] Natalini R., Convergence to equilibrium for the relaxation approximations of conservation laws. *Comm. Pure Appl. Math.*, **49**:795–823, 1996.

[29] Ngoduy D., Hoogendoorn S.P. and Liu R., Continuum modeling of cooperative traffic flow dynamics, *Physica A: Statistical Mechanics and its Applications*, **388**:2705-2716, 2009.

[30] Ngoduy D., Application of gas-kinetic theory to modeling mixed traffic of manual and ACC vehicles, *Transpormetrica*, **8**:43-60, 2012.

[31] Ngoduy D., 2013. Platoon based macroscopic model for intelligent traffic flow, *Transportmetrica, Part B*, **1**:153-169, 2013.

[32] Ngoduy D., Instability of cooperative adaptive cruise control traffic flow: A macroscopic approach, *Commun. Nonlinear Sci Numer Simulat.*, **18**:2838-2851, 2013.

[33] Ngoduy D. and Wilson R.E., Multi-anticipative non-local macroscopic traffic model. *Computer-Aided Civil and Infrastructure Engineering*, **29**:248-263, 2014.

[34] Nowakowski C., Shladover S.E., Cody D., Bu F., OConnell J., Spring J., Dickey S. and Nelson D., Cooperative Adaptive Cruise Control: Testing Drivers Choices of Following Distances. Research Report. PATH, University of California, 2011.

[35] Ntousakis I.A., Porfyri K., Nikolos I.K, and Papageorgiou M., Assessing the impact of a cooperative merging system on highway traffic using a microscopic flow simulator, Proceedings of the ASME International Mechanical Engineering Conference & Exposition, IMECE2014, Nov. 14-20, Montreal, Quebec, Canada, Paper No. IMECE2014-39850, 2014.

[36] Ntousakis I.A., Nikolos I.K, and Papageorgiou M., On microscopic modeling of Adaptive Cruise Control systems, 4th International Symposium of Transport Simulation, ISTS 2014, Corsica, France, June 1-4, 2014.

[37] Pareschi L. and Russo G., Implicit-explicit Runge-Kutta schemes and applications to hyperbolic systems with relaxation *J. Sci. Comput.*, **25**(1):129-155, 2005.

[38] Seaid M., Improved Applications of Relaxation Schemes for Hyperbolic Systems of Conservation Laws and Convection-Diffusion Problems, *Comp. Meth. Appl. Math.* **6**(2):56-86, 2006.

[39] Seaid M., Stable numerical methods for conservation laws with discontinuous flux function, *Applied Mathematics and Computation*, **175**:383-400, 2006.

[40] Shen W., Zhang C. and Zhang J., Relaxation method for unsteady convection-diffusion equations, *Comput. Math. Appl.*, **61**:908-920, 2011.

[41] Shladover S.E., Lu X.Y., Cody D., Nowakowski C., Qiu Z.T., Chow A., O'Connell J., Nienhuis J., and Su, D. Development and Evaluations of Selected Mobility Applications for VII: Concept of Operations PATH Research Report, 2010.

[42] Shladover S.E., Su D. and Lu X.-Y., Impacts of Cooperative Adaptive Cruise Control on Freeway Traffic Flow, *Transp. Res. Rec. J. Transp. Res. Board*, 2324, 6370, 2012.

[43] Swaroop D. and Rajagopal K.R., Intelligent Cruise Control Systems and Traffic Flow Stability, *Transportation Research C*, **7**:329-352, 1999.

[44] Treiber M., Hennecke A. and Helbing D., Derivation, properties, and simulation of a gas-kinetic-based, nonlocal traffic model, *Physical Review E - Statistical Physics, Plasmas, Fluids, and Related Interdisciplinary Topics*, **59**(1):239-253, 1999.

[45] Treiber M. and Helbing D., Macroscopic simulation of widely scattered synchronized traffic states, *J. Phys. A: Math. Gen*, **32**:17-23, 1999.

[46] Treiber M., Kesting A. and Helbing D., Three-phase traffic theory and two-phase models with a fundamental diagram in the light of empirical stylized facts, *Transportation Research Part B*, **44**:983-1000, 2010.

[47] Treiber M. and Kesting A. Traffic flow dynamics: Data, models and simulation, Springer, 2013.

[48] van Arem B., van Driel C. and Visser R., The Impact of Cooperative Adaptive Cruise Control on Traffic-Flow Characteristics. Proceedings of the IEEE Transaction, Intelligence Transportation System, **7**:429-436, 2006.

[49] VanderWerf J., Shladover S.E., Miller M.A. and Kourjanskaia N., Evaluation of the Effects of Adaptive Cruise Control Systems on Highway Traffic Flow Capacity and Implications for Deployment of Future Automated Systems. Transportation Research Record, **1800**:78-84, 2002.

[50] Witham G.B., Linear and nonlinear waves, John Wiley and Sons, New York, 1974

[51] Yi J. and Horowitz R., Macroscopic traffic flow stability for Adaptive Cruise Controlled (ACC) vehicles, in Proceedings of the 41st IEEE Conference on Decision and Control, Las Vegas Nevada, USA, 2002